Title

Microglia drive experience-dependent spine plasticity and extracellular matrix remodeling in response to neuron-derived Interleukin-33

Permalink

https://escholarship.org/uc/item/59r9k8b6

Author

Nguyen, Phi Tan

Publication Date

2021

Peer reviewed|Thesis/dissertation

Microglia drive experience-dependent spine plasticity and extracellular matrix remodeling in response to neuron-derived Interleukin-33

by
Phi Nguyen

DISSERTATION
Submitted in partial satisfaction of the requirements for degree of
DOCTOR OF PHILOSOPHY

in

Biomedical Sciences

in the

GRADUATE DIVISION
of the
UNIVERSITY OF CALIFORNIA, SAN FRANCISCO

Approved:

DocuSigned by:
_Eric Huang_____   Eric Huang
9A805C3F0428410...   Chair

DocuSigned by:
_Mr. K._____   Mazen Kheirbek
DocuSigned by...33...
_Roger Nicoll_____   Roger Nicoll
DocuSigned by...430...
_Anna Molofsky_____   Anna Molofsky
7148719D502F43A...

_____
                                                        Committee Members

Acknowledgments

First, I would like to thank my parents, Phuoc and Tho Nguyen, and my sister, Thao. From emigrating from post-war Vietnam and starting over in a new country to working multiple jobs to raise my sister and I, their work ethic and resilience have been inspiring to me. Without my family's collective sacrifices, I would not have had the opportunity to attend college or pursue a PhD. Their strength has inspired me throughout my PhD and helped me to remain grounded in challenging circumstances.

I would also like to thank my wife, Charlie. She has provided endless support and encouragement during the highs and lows of graduate school. She is someone that I knew I could always rely on when I needed help or advice. Despite battling and beating her own cancer diagnosis, she is always looking to help others first. Her strength was and continues to be an incredible inspiration for me.

I would also like to thank my PI, Anna Molofsky, for her guidance and support over the past five years. Anna taught me to trust my instincts and explore data in ways that helped uncover unexpected findings. She gave me a new appreciation for glia biology and science in general. Anna worked tirelessly to keep the lab running smoothly, which freed me to discover and pursue my curiosity. I also want to thank the members of the Molofsky lab for their patience, expertise, and support.

I also want to thank the members of my thesis committee – Roger Nicoll, Eric Huang, and Mazen Kheirbek. They have supported me throughout my PhD and provided critical feedback and new perspectives on science.

Contributions

This manuscript contains data originally published in the following report:

Nguyen PT, Dorman LC, Pan S, Vainchtein ID, Han RT, Nakao-Inoue H, Taloma SE, Barron JJ, Molofsky AB, Kheirbek MA, Molofsky AV. Microglia remodeling of the extracellular matrix promotes synapse plasticity. *Cell.* Vol 182, Issue 2, 388-40 (2020)

Abstract

Microglia drive experience-dependent spine plasticity and extracellular matrix remodeling in response to neuron-derived Interleukin-33

Phi T. Nguyen

Synapse remodeling is essential to encode experiences into neuronal circuits. Here we define a molecular interaction between neurons and microglia that drives experience-dependent synapse remodeling in the hippocampus. We find that the cytokine Interleukin-33 (IL-33) is expressed by adult hippocampal neurons in an experience-dependent manner and defines a neuronal subset primed for synaptic plasticity. Loss of neuronal IL-33 or the microglial IL-33 receptor leads to impaired spine plasticity, reduced newborn neuron integration, and diminished precision of remote fear memories. Memory precision and neuronal IL-33 are decreased in aged mice, and IL-33 gain of function mitigates age-related decreases in spine plasticity. We find that neuronal IL-33 instructs microglial engulfment of extracellular matrix (ECM), and that its loss leads to impaired ECM engulfment and a concomitant accumulation of ECM proteins in contact with dendritic spines. These data define a cellular mechanism through which microglia regulate experience-dependent synapse remodeling and promote memory consolidation.

Table of Contents

List of Figures

Chapter 1: Introduction

Neural circuits undergo ongoing structural changes in synaptic connectivity in response to experience. Defining the mechanisms of these remodeling processes is critical to understanding how experiences become stably encoded in the brain. Components of the innate immune system regulate synapse formation and stabilization (Bennett and Molofsky, 2019; Kaneko et al., 2008; Lee et al., 2014; Stevens et al., 2007). Consistent with this, microglia, the predominant immune cells within the brain parenchyma, have been increasingly implicated in synapse remodeling. Microglia make ongoing and activity-dependent contact with dendritic spines (Eyo et al., 2014, 2015; Li et al., 2012; Madry et al., 2018; Tremblay et al., 2010; Wake et al., 2009). They engulf synapse components during early thalamic development and in the hippocampus (Paolicelli et al., 2011; Schafer et al., 2012; Vainchtein et al., 2018; Wang et al., 2020). However, microglia can also promote spine formation in an experience-dependent manner (Miyamoto et al., 2016; Parkhurst et al., 2013) and are required for some forms of cortical plasticity (Sipe et al., 2016). These data suggest that communication between neurons and microglia regulates synaptic plasticity.

However, the mechanisms by which these activity-dependent contacts lead to stable changes in synaptic connectivity are unknown. This is in part because molecules known to regulate microglial function are only beginning to be studied and have been challenging to examine with cell-type specific manipulations. Our group recently identified the IL-1 family cytokine Interleukin-33 (IL-33) as a novel regulator of microglial activation

and function (Vainchtein et al., 2018). IL-33 is normally sequestered in the nucleus in an inactive state, but upon release into the extracellular space is a potent activator of NF-κB signaling in target cells that express its obligate receptor, IL1RL1 (a.k.a. ST2; (Molofsky et al., 2015)). We found that during early postnatal development, IL-33 expressed by astrocytes in the developing thalamus and spinal cord drove microglial synapse engulfment and restricted excitatory synapse numbers.

Synapse remodeling continues throughout life in brain regions that change in response to learning and experience. This is particularly relevant in the hippocampus, a brain region essential for learning and memory consolidation. Here we define a mechanism by which neuron-microglia signaling via IL-33 augments synaptic plasticity in the hippocampus in an experience-dependent manner. We found that neurons were the predominant source of IL-33 in this region and that microglia expressed the IL-33 receptor IL1RL1. *Il33* expression in hippocampal neurons defined a molecularly distinct subset of neurons that expressed markers of synaptic plasticity and *Il33* expression in these neurons was responsive to experience. Conditional deletion of *Il33* from neurons or its receptor from microglia resulted in fewer dendritic spines as well as spine head filopodia, a marker of spine plasticity. Conversely, viral-mediated IL-33 gain-of-function was sufficient to increase spine formation. Loss of this signaling pathway resulted in fewer newborn neurons in the dentate gyrus and impairments in precise retrieval of remote fear memory. Aging was associated with a substantial decrease in neuronal IL-33 as well as deficits in memory precision at both recent and remote timepoints. IL-33 gain of function mitigated age-related declines in spine plasticity and neuronal activation.

Finally, we demonstrate that IL-33 directly promotes microglial engulfment of extracellular matrix proteins. IL-33 induced a microglial transcriptional program consistent with activation, phagocytosis, and ECM remodeling. IL-33 was necessary and sufficient for microglial engulfment of Aggrecan, a chondroitin sulfate proteoglycan highly enriched in the dentate gyrus. Loss of IL-33 led to an accumulation of ECM proteins in the IL-33 deficient hippocampus, particularly around synapses and dendritic spines. Exogenous enzymatic clearance of ECM was sufficient to restore dendritic spine numbers after neuron-specific deletion of IL-33, directly linking IL-33's impact on spines to its role in remodeling the ECM. Taken together, these studies reveal a molecular mechanism linking microglial remodeling to neuronal experience and demonstrate that this pathway is required for the precise consolidation of long-term memories.

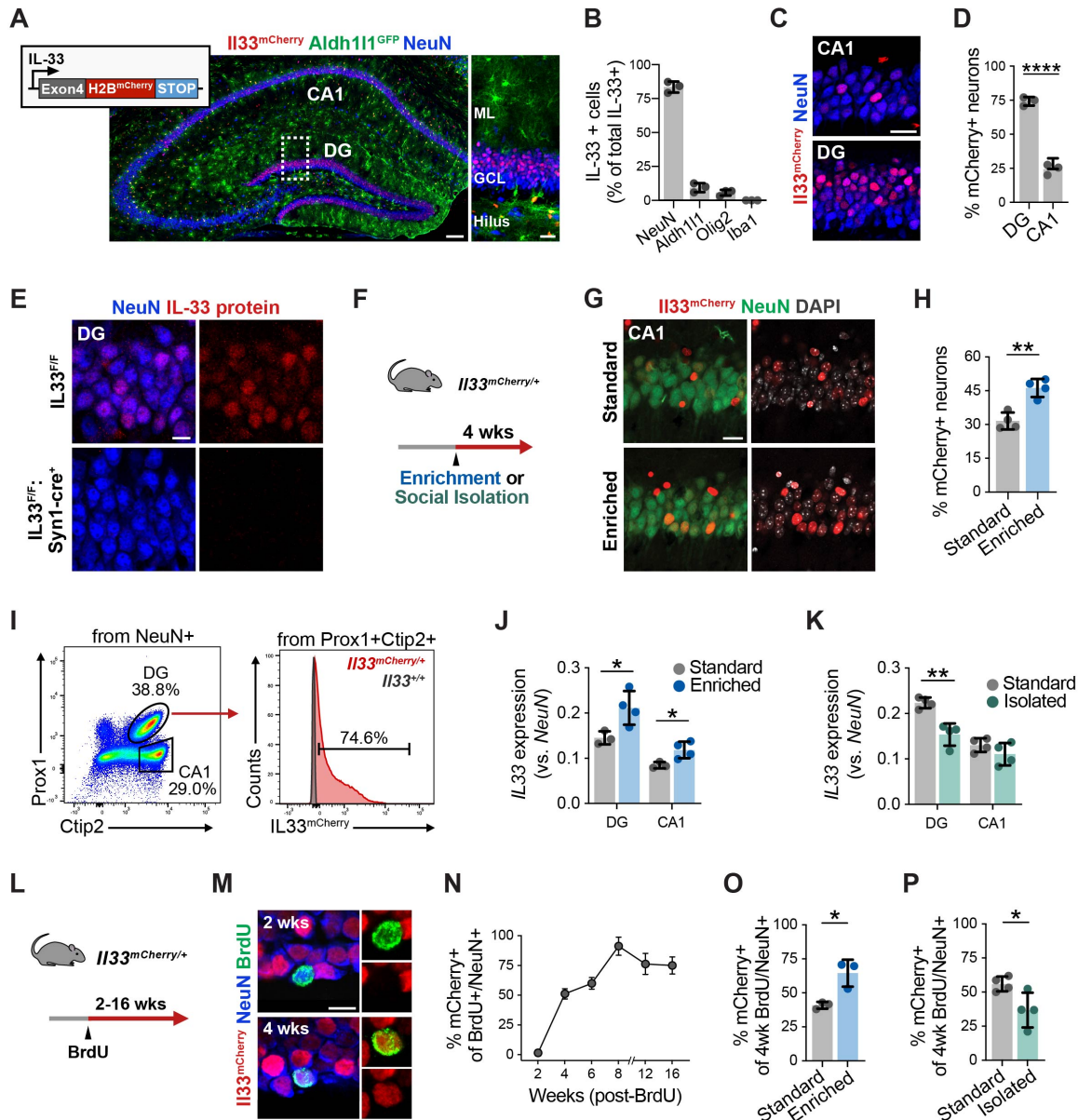# Chapter 2: Experience-dependent regulation of *Il33* expression in adult hippocampal neurons

To identify the cellular sources of IL-33 in the hippocampus we used a nuclear localized knock-in reporter line (*Il33^{mCherry/+}*, **Fig. 2.1A**). Unlike in developing subcortical regions, where *Il33* is primarily expressed by astrocytes (Vainchtein et al., 2018), we found that most Il33-mCherry expressing cells in the hippocampus were neurons **(Fig. 2.1A-B, Fig. 2.2A**). *Il33* has two isoforms that produce the same protein but are regulated by alternate promoters (Talabot-Ayer et al., 2012). We found that neurons expressed the *Il33b* isoform, whereas astrocytes produced *Il33a*, suggesting that neurons may have unique regulatory mechanisms for IL-33 production (**Fig. 2.2B**). Il33-mCherry was expressed by 74% of neurons in the dentate gyrus (DG) and 24% of neurons in the CA1 subregion (**Fig. 2.1C-D).** Within the DG, *Il33* was expressed in Prox1+ granule cells, but not PV+ interneurons, and rarely in Doublecortin+ immature granule cells (**Fig. 2.2C-D**). We did not detect neuronal *Il33* expression in entorhinal cortex, amygdala, thalamus, or other subcortical regions, although some neurons in layer 2/3 of prefrontal cortex also expressed *Il33* **(Fig. 2.2E**). These results were validated by immunostaining for IL-33 protein, which demonstrated neuronal expression of IL-33 and was abrogated by conditional deletion with a neuron-specific *Syn1^{Cre}* recombinase line ('IL-33 cKO'; **Fig. 2.1E**). As in glia and other cell types, we found that native IL-33 was primarily nuclear-localized (**Fig. 2.1E**, **Fig. 2.2F**; (Vainchtein et al., 2018)).

We observed that *Il33* was enriched in hippocampal regions that undergo robust experience-dependent remodeling. To determine whether *Il33* expression is regulated by

experience, three month old $Il33^{mCherry/+}$ mice were placed in an enriched environment (EE), an intervention that promotes circuit remodeling, spine formation, and neurogenesis (**Fig. 2.1F**; (Bednarek and Caroni, 2011; Bergami et al., 2015; Kempermann et al., 1997)). We observed that 4 weeks of enrichment led to a significant increase in the total number of Il33-mCherry+ CA1 neurons (**Fig. 2.1G-H**). To further examine this, we isolated neuronal nuclei by flow cytometry from both DG granule cells ($Prox1^+Ctip2^+$) and CA1 pyramidal neurons ($Prox1^+Ctip2^-$; **Fig. 2.1I,** (Jaeger et al., 2018; Lacar et al., 2016)). Enrichment increased $Il33$ mRNA expression in both the DG and CA1 (**Fig. 2.1J**) and increased the percentage of Il33-mCherry+ neurons in CA1 over a period of 14 days (**Fig. 2.2G-I**). In contrast to enrichment, social isolation reduces hippocampal remodeling and impairs neurogenesis (Dranovsky et al., 2011; Ibi et al., 2008). We found that four weeks of social isolation post-weening significantly reduced $Il33$ mRNA expression and the percentage of neurons that were Il33-mCherry+ in the DG (**Fig. 2.1K, Fig. 2.2J**). Additionally, we detected a small proportion of Il33-mCherry+ neurons in the CA2 region and this proportion increased with enrichment. Conversely, Il33-mCherry+ neurons were rarely detected in CA3 (**Fig. 2.2K-L**).

The dentate gyrus undergoes neurogenesis and integration of newborn neurons, which are modulated by experience (Alvarez et al., 2016; Bergami et al., 2015; Kempermann et al., 1997). To determine if $Il33$ expression was induced in adultborn neurons, we injected Bromodeoxyuridine (BrdU) into one-month old $Il33^{mCherry/+}$ mice to label newborn neurons (**Fig. 2.1L**). We found that $Il33$ was induced in newborn neurons between 2-4 weeks post-BrdU (**Fig. 2.1M-N).** Additionally, environmental enrichment in

adult (3-month-old) mice significantly increased the proportion of 4-week-old Il33-mCherry+ newborn neurons (**Fig. 2.1O**). In contrast, when mice were placed into social isolation post-weaning, the proportion of Il33-mCherry+ newborn neurons was significantly decreased (**Fig. 2.1P**). Taken together, these results demonstrate that *Il33* expression in hippocampal neurons can increase in response to experiences known to promote neurogenesis and spine formation, which are key aspects of circuit remodeling (Alvarez et al., 2016; Bergami et al., 2015; Kempermann et al., 1997), and that *Il33* expression decreases in settings where neurogenesis is diminished (Ibi et al., 2008).

Figure 2.1: Experience-dependent regulation of IL-33.

(A-B) Representative image and quantification of P30 hippocampus of a double reporter line showing Il33^{mCherry}, Aldh1l1^{eGFP} (astrocytes), and NeuN (neurons). Inset shows dentate gyrus (DG). Quantification of % of IL-33 positive cells that are labeled with cell type specific markers across the entire DG. Scale: 100 μm, 20 μm (inset). *ML*, molecular layer; *GCL*, granule cell layer.

(C-D) Image and quantification of neuronal IL-33 in DG and CA1. Scale: 20 μm.

(E) IL-33 protein in DG neurons in control animals (top, *Il33$^{fl/fl}$*) or after neuron-specific excision of *Il33* (bottom, *Il33$^{fl/fl}$*: Synapsin1-cre). Scale bar: 10 μm.

(F) Schematic of environmental enrichment and social isolation paradigms.

(G-H) Representative image of CA1 from *Il33^{mCherry}* reporter in standard or enriched conditions, and quantification by immunohistochemistry. Scale bar: 20 μm.

(I) FACS gating strategy for isolation of Il33-mCherry+ neurons from DG and CA1.

(J-K) Impact of enrichment or social isolation on *Il33* expression by qPCR.

(L) Schematic of newborn neuron labeling with BrdU injections in 4-week old animals.

(M-N) Representative image and quantification of the percentage of Il33-mCherry+ newborn neurons at indicated time-points after BrdU injection (n = 3 mice per timepoint; at least 20 neurons per mouse). All mice were injected at 4 weeks of age. Scale bar: 10 μm.

(O) Impact of enrichment on percentage of Il33-mCherry+ newborn neurons. Mice were pulse-labeled with BrdU and enriched at 3 months of age and then analyzed four weeks later.

(P) Impact of social isolation on percentage of Il33-mCherry+ newborn neurons. Mice were pulse-labeled with BrdU and socially isolated post-weaning at 1 month of age and then analyzed four weeks later.

Statistics: two-tailed unpaired t-tests. Dots represent individual mice, data represented as mean ± standard deviation.*p < 0.05, **p < 0.01, ***p < 0.001.
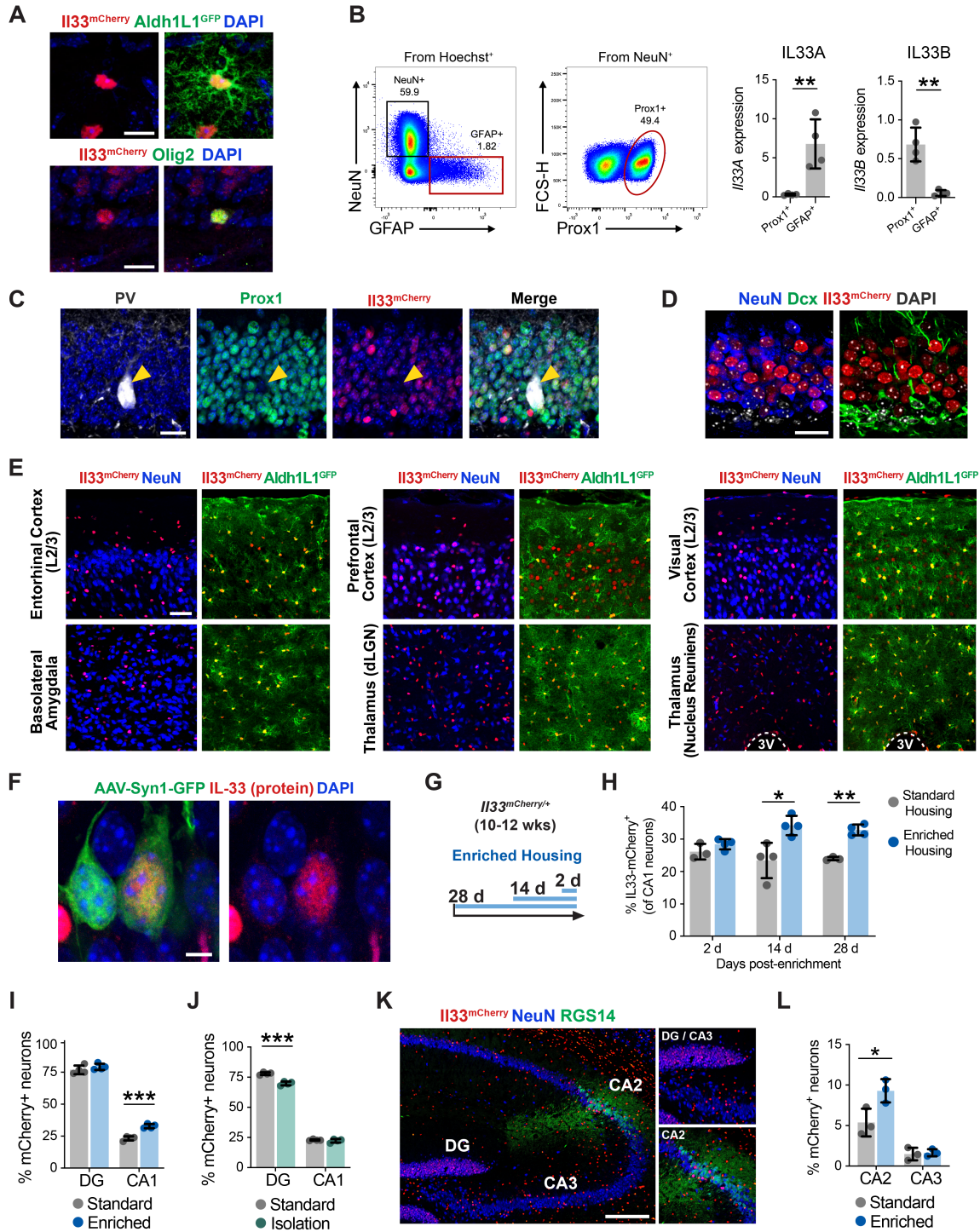
Figure 2.2: IL33 expression across the brain.
(A) *Il33* expression (Il33-mCherry) in hippocampal astrocytes (Aldh1l1-GFP) and oligolineage cells (Olig2). Scale bar: 10 μm.
(B) Representative gating and expression of *Il33* transcript isoforms from qPCR of flow sorted hippocampal astrocytes and dentate granule cells (t-test, n = 4 mice).

(C) DG neurons with immunolabeling for Il33-mCherry, the granule cell marker Prox1, and interneuron marker parvalbumin (PV). Scale bar: 20 μm.

(D) DG neurons with immunolabeling for Il33-mCherry, NeuN, and the progenitor/immature neuron marker Doublecortin (Dcx). Scale bar: 10 μm.

(E) Expression of Il33-mCherry with the astrocyte reporter Aldh1l1-eGFP and NeuN across brain regions in adult mice. Scale bar: 50 μm. 3V: third ventricle.

(F) Immunostaining for IL-33 protein and neuronal labeling with AAV9-Syn1-GFP. Scale bar: 5 μm.

(G-H) Schematic and timecourse of the percentage of Il33-mCherry+ neurons in the CA1 region after indicated time periods of environmental enrichment quantified by flow cytometry (2-way ANOVA, Tukey's post hoc test, n = 3-4 mice/group).

(I) Proportion of Il33-mCherry+ neurons in DG and CA1 after 4 weeks of enrichment vs standard housing quantified by flow cytometry (t-test; n = 4 mice).

(J) Proportion of Il33-mCherry+ neurons after 4 weeks of social isolation vs standard housing quantified by flow cytometry (t-test; n = 4 mice).

(K-L) Percentage of NeuN+ neurons that are Il33-mCherry+ after 4 weeks of enrichment vs standard housing in the CA2 region, as demarcated by RGS14 staining, and CA3 (t-test, n = 3 mice/condition). Scale bar: 200 μm.

*p<0.05, **p<0.01, ***p<0.001. Data = mean ± SD.

Chapter 3: *Il33* identifies a neuronal subset primed for synaptic plasticity

Memory encoding and consolidation are highly circuit-specific and competitive processes (Josselyn and Tonegawa, 2020). We observed that DG neurons expressed heterogeneous levels of IL-33 (**Fig. 2.1E**). To determine whether this heterogeneity had functional correlates, we performed single-nucleus RNA-sequencing of hippocampal neuronal nuclei using the 10x single cell gene expression platform (**Fig. 3.1A-F, Fig. 3.2A-F**). Unbiased clustering revealed cell subsets corresponding to dentate granule cells (expressing *Prox1, Stxbp6, Dock10*), as well as other major hippocampal neuron classes (**Fig. 3.1A, Fig. 3.2D-E**). The DG population further clustered into two subsets, clusters 0 and 2 (**Fig. 3.1B).** To identify *Il33*+ subsets, we also sequenced flow sorted *Il33^mCherry^+* neurons and included this metadata in our clustering analyses, where we found that the majority of Il33-mCherry+ neurons clustered with DG cluster 2 (**Fig. 3.1C-D, Fig. 3.2F-G**). Thus, IL-33 marks a molecularly distinct subset of DG neurons.

To define the genes that segregate these clusters, we ranked differentially expressed genes between these subsets within the DG (**Fig. 3.1E-F**; (Finak et al., 2015)). *Il33*+ neurons were highly enriched for genes linked to cell adhesion, synapse assembly, and synaptic plasticity including cadherins (*Cdh10, Cdh13* (Basu et al., 2017; Duan et al., 2018))*,* and others (*Negr1*, *Tenm2 Dcc, Sorcs2, Myo5b*). We also found enriched expression of genes related to assembly and remodeling of the extracellular matrix (ECM) including *Adamts9, Itga4, Col23a1,* and *Col25a1*. As these genes are not well annotated

in current gene ontology classifications, we cross-referenced our data with a curated dataset of matrix-associated genes ((Naba et al., 2016), **Fig. 3.1E,** green dots) and identified 18 upregulated genes encoding ECM-associated proteins. Thus, *Il33* expression defines a molecular subtype enriched for markers of synapse formation and ECM remodeling.

We next investigated whether *Il33* expression correlated with structural and functional markers of synaptic plasticity. In the hippocampus, dendritic spines and synapses remodel dynamically and in response to experience (Adlaf et al., 2017; Attardo et al., 2015; Bergami et al., 2015; McAvoy et al., 2016; Pfeiffer et al., 2018; Ryan et al., 2015). DG granule cells recruited to encode a memory undergo a period of enhanced plasticity and spine growth that is required for proper memory consolidation (Kitamura et al., 2017; Roy et al., 2017; Ryan et al., 2015). We quantified dendritic spines in sparsely labeled mature dentate granule cells in *Il33$^{mCherry/+}$* mice and compared neurons with different levels of *Il33* expression (**Fig. 3.1G**). Compared to neurons with low levels of Il33-mCherry intensity, we found that neurons with high mCherry had increased dendritic spine density, as analyzed by binning neurons into three groups (**Fig. 3.1H**), or by Pearson correlation (**Fig. 3.2H**). We also quantified spine head filopodia as a structural marker of spine plasticity. These spine protrusions form prior to new spine formation or spine relocation and have been observed in the olfactory bulb and CA1 regions (Breton-Provencher et al., 2016; Orlando et al., 2012; Richards et al., 2005; Weinhard et al., 2018). We identified spine head filipodia in the DG and found that neurons with high Il33-mCherry levels had a significantly greater proportion of spines harboring spine head

filopodia (**Fig. 3.1I-J; Fig. 3.2I**).

The expression of immediate early genes such as *Cfos* and *Arc* identifies neuronal ensembles recruited during the encoding of contextual memories (Denny et al., 2014; Liu et al., 2012). These neuronal populations are allocated to a specific memory trace in a competitive process based on their relative excitability, among other properties (Cai et al., 2016; Han et al., 2007; Park et al., 2016; Pignatelli et al., 2019). To determine if *Il33*-high neurons were more likely to be activated in response to learning, we placed animals in a novel environment for one hour and found that neuronal subsets with higher *Il33* expression were more likely to express c-Fos protein than *Il33*-low subsets (**Fig. 3.1K-L**), suggesting that this *Il33*-high pool may be functionally distinct. However, the total number of c-Fos+ DG neurons did not differ in IL-33 cKO mice (**Fig. 3.2J**), suggesting that IL-33 does not control the size of an engram population. Rather, our data indicate that a subset of neurons with high *Il33* expression are more likely to engage in response to novel experiences. Altogether, our transcriptomic and structural data suggest that *Il33* expression is associated with a subset of neurons more likely to undergo synaptic remodeling.
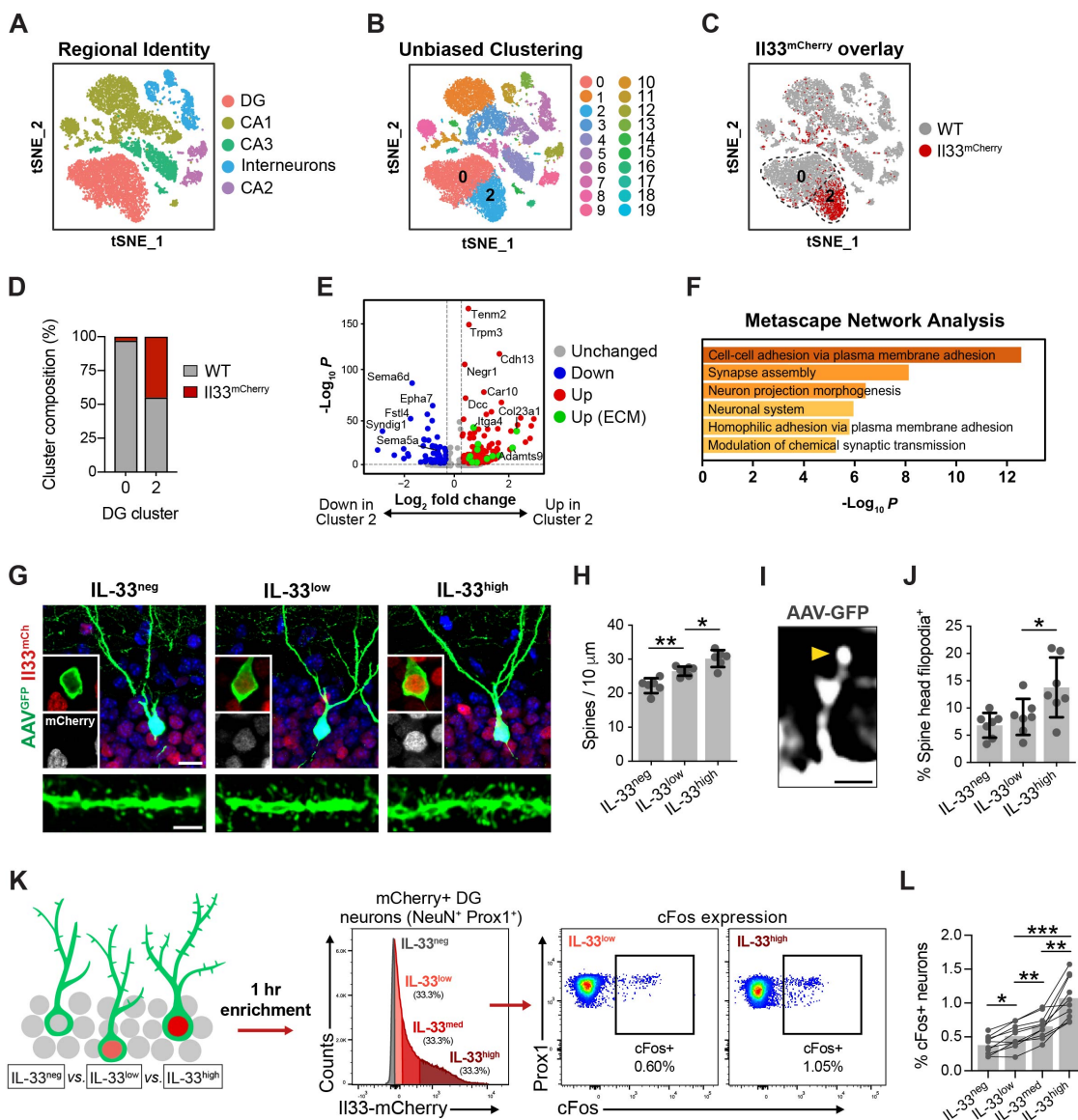
Figure 3.1: IL-33 marks neurons primed for synaptic plasticity.

(A) 10,800 FACS purified NeuN+ nuclei were sequenced using the 10x Chromium single cell expression system, visualized with t stochastic nearest neighbor embedding (tSNE) and labeled by hippocampal cell type assignment (see also Figure S2).

(B) Unsupervised clustering of data presented in A.

(C) WT nuclei (gray) overlaid with sequenced *Il33^{mCherry}*+ nuclei (red).

(D) Quantification of WT vs *Il33^{mCherry}*+ DG clusters 0 and 2.

(E) Volcano plot of differentially expressed genes between DG cluster 2 (*Il33*+) and DG cluster 0 calculated with MAST (p < 0.001). Green dots highlight ECM and ECM-interacting genes from the Matrisome database (Naba et al., 2016).

(F) Metascape network analysis of upregulated genes in E shows top gene ontology terms.

(G) Representative images of dentate granule cells sparsely labeled with AAV$_9$-Synapsin1-GFP from adult *Il33$^{mCherry/+}$* mice showing IL-33^{neg}, IL-33^{low}, and IL-33^{high} subsets. AAV was injected intracerebroventricularly at P2. Scale bar: 10 μm (top), 2 μm (bottom).

(H) Dendritic spine density in IL-33 negative, low, and high neuron subpopulations (ANOVA, $p < 0.0001$, Tukey's post-hoc test, n = 6-7 neurons/group, 3 mice).

(I-J) Representative image of dendritic spine harboring a spine head filopodia and quantification of the percentage of spines with spine head filopodia (ANOVA, $p = 0.0096$, Tukey's post-hoc test, n = 6-7 neurons/group, 3 mice). Scale bar: 1 μm.

(K) Schematic and FACS plots showing gating strategy for isolating neuronal nuclei by mCherry intensity and subsequent quantification of the percentage of cFos+ cells 1 hour after exposure to a novel environment. IL-33 low, medium, and high groups each comprised of 33% of the Il33-mCherry+ population.

(L) Quantification of the percentage of cFos+ cells in each group (Repeated measures ANOVA, $p < 0.0001$, Tukey's post-hoc test, n = 10 mice).

*$p < 0.05$, **$p < 0.01$, ***$p < 0.001$. Data in G-L represented as mean ± standard deviation. See full methods for statistical details in A-F.
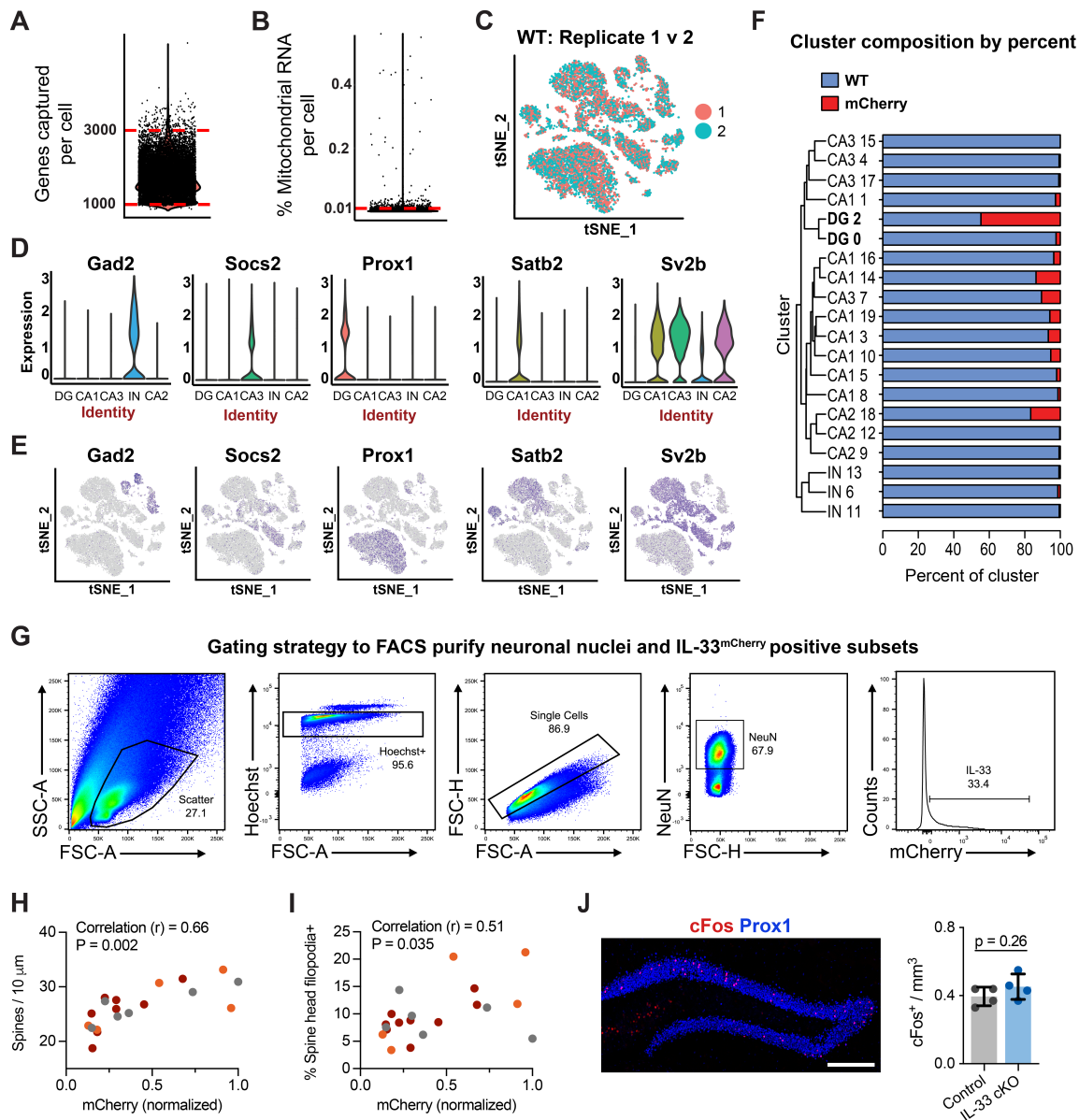
Figure 3.2: Validation of single nucleus RNA sequencing.
(A-B) Quality control metrics for single nuclei RNA sequencing. (A) Number of genes recovered per cell. (B) Mitochondrial RNA content per cell. Lines show thresholds used for cell selection prior to all other analyses.
(C) t-SNE plot showing clustering of the independent wild-type replicates (coral and turquoise).
(D-E) Violin and t-SNE plots of markers used to assign subtype identities (**Fig. 2B**) showing genes for interneurons (Gad2), CA3 pyramidal neurons (Socs2), DG granule cells (Prox1), CA1 pyramidal neurons (Satb2), and CA2/CA region pyramidal neurons (Sv2b).
(F) Percentage of cells per cluster originating from WT (blue) and Il33-mCherry (red) samples.

(G) Gating strategy to isolate neuronal nuclei and Il33-mCherry nuclei for single-cell RNA sequencing.

(H-I) Correlation between mCherry levels and dendritic spine or spine head filopodia numbers (Pearson correlation, n = 20 neurons, >110 spines per neuron, 3 mice). Different colors correspond to neurons from individual mice.

(J) Representative image and quantification of the number of cFos+ cells in the

Chapter 4: Neuron-microglial signaling via IL-33 drives experience-dependent spine remodeling

To identify potential cellular targets of IL-33 signaling we quantified expression of *Il1rl1*, which encodes its obligate co-receptor (Molofsky et al., 2015; Palmer and Gabay, 2011). Microglia were the predominant cell type expressing *Il1rl1* in the hippocampus, as assessed by qPCR of cell subsets isolated by flow cytometry (**Fig. 4.2A-B**), and consistent with other regions of the CNS (Vainchtein et al., 2018). Quantitative *in situ* hybridization supported these results, although we also identified a small proportion of *Il1rl1*+NeuN+ cells in the hilus (**Fig. 4.1A-B**). Genetic deletion of *Il1rl1* with a myeloid-specific inducible *Cre* recombinase line (*Il1rl1^{flox/flox}:Cx3cr1^{CreER/+}* 'IL1RL1 i-cKO') led to a 93% ± 5.6% percent reduction in *Il1rl1* expression in microglia (**Fig. 4.2C-D**). Thus, microglia express the obligate IL-33 receptor *Il1rl1* and are competent to respond to IL-33 signaling.

Given the strong enrichment in markers of synapse formation in IL-33+ neurons, we next investigated whether neuronal IL-33 or microglial IL1RL1 impacted hippocampal dendritic spine numbers. We quantified dendritic morphology and spine density in mice with neuron-specific deletion of *Il33* (*Il33^{flox/flox}:Syn1^{Cre}* 'IL-33 cKO') using AAV9-Syn1-GFP sparse labeling of hippocampal neurons (**Fig. 4.1C**). We found that dendritic spine density was significantly decreased after loss of neuronal IL-33 in both the DG and CA1 regions (**Fig. 4.1D; Fig. 4.2E**), although dendritic branching was largely preserved (**Fig. 4.2F**). Conditional deletion of the IL-33 receptor *Il1rl1* in microglia at 4 weeks of age

(*Il1rl1flox/flox:Cx3cr1CreER/+* 'IL1RL1 i-cKO') phenocopied the decreased spine density seen with deletion of IL-33 from neurons (**Fig. 4.1E**). Numbers of microglia were not altered in these mice (**Fig. 4.2G**), suggesting alterations in microglial function. Consistent with this, mice with constitutive deletion of *Il1rl1* (*Il1rl1flox/flox:Cx3cr1Cre/+* 'IL1RL1 cKO') had decreased microglial process coverage in the molecular layer of the DG (**Fig. 4.2H**).

Microglial contact has been correlated with the formation of new dendritic spines and the induction of spine head filopodia (Miyamoto et al., 2016; Weinhard et al., 2018). We quantified spine head filopodia in DG neurons and found that loss of neuronal IL-33 or microglial IL1RL1 resulted in significantly fewer spines with spine head filopodia (**Fig. 4.1F-H**). Environmental enrichment significantly increased the number of spine head filopodia in control mice, whereas constitutive deletion of *Il1rl1* from microglia limited this increase (**Fig. 4.1I-J**). To determine the impact of these spine alterations on synaptic function, we performed whole cell patch clamp recordings of DG granule cells from IL-33 cKO animals and littermate controls. We found a reduction in the frequency of miniature excitatory postsynaptic currents (mEPSCs) in IL-33 cKO animals and an increase in the amplitude of these mEPSCs (**Fig. 4.1K-M**). These data are consistent with our finding of fewer dendritic spines and suggests strengthening of the remaining spines. Taken together, these data suggest that neuron-microglial signaling via IL-33 promotes new spine formation and plasticity.

To determine whether IL-33 signaling through microglia is sufficient to drive spine formation we next used a gain-of-function approach. In order to drive constitutive release

of IL-33, we removed the N-terminal chromatin-binding domain containing the nuclear localization signal (NLS) and replaced it with an HA epitope tag (Bessa et al., 2015). We then used lentiviral delivery to express this modified protein (LV-CaMKII-IL33 NLS-P2A-tdTomato) or control (LV-CaMKII-tdTomato) in DG neurons (**Fig. 4.1N**). We were able to detect cytoplasmic and dendritic HA-tagged IL-33 protein, indicating that the construct was functioning as expected (**Fig. 4.2I**). We found that IL-33 gain-of-function in neurons was sufficient to increase dendritic spine numbers and spine head filopodia, and that these effects were abrogated in IL1RL1 i-cKO mice, indicating that microglial sensing of IL-33 was required (**Fig. 4.1O-Q**). Furthermore, our gain-of-function results suggest that IL-33 acts locally to increase dendritic spines, although non-cell autonomous effects of IL-33 release on nearby neurons are also possible. Taken together, however, these data indicate that IL-33 release from neurons is sufficient to promote dendritic spine formation and plasticity.
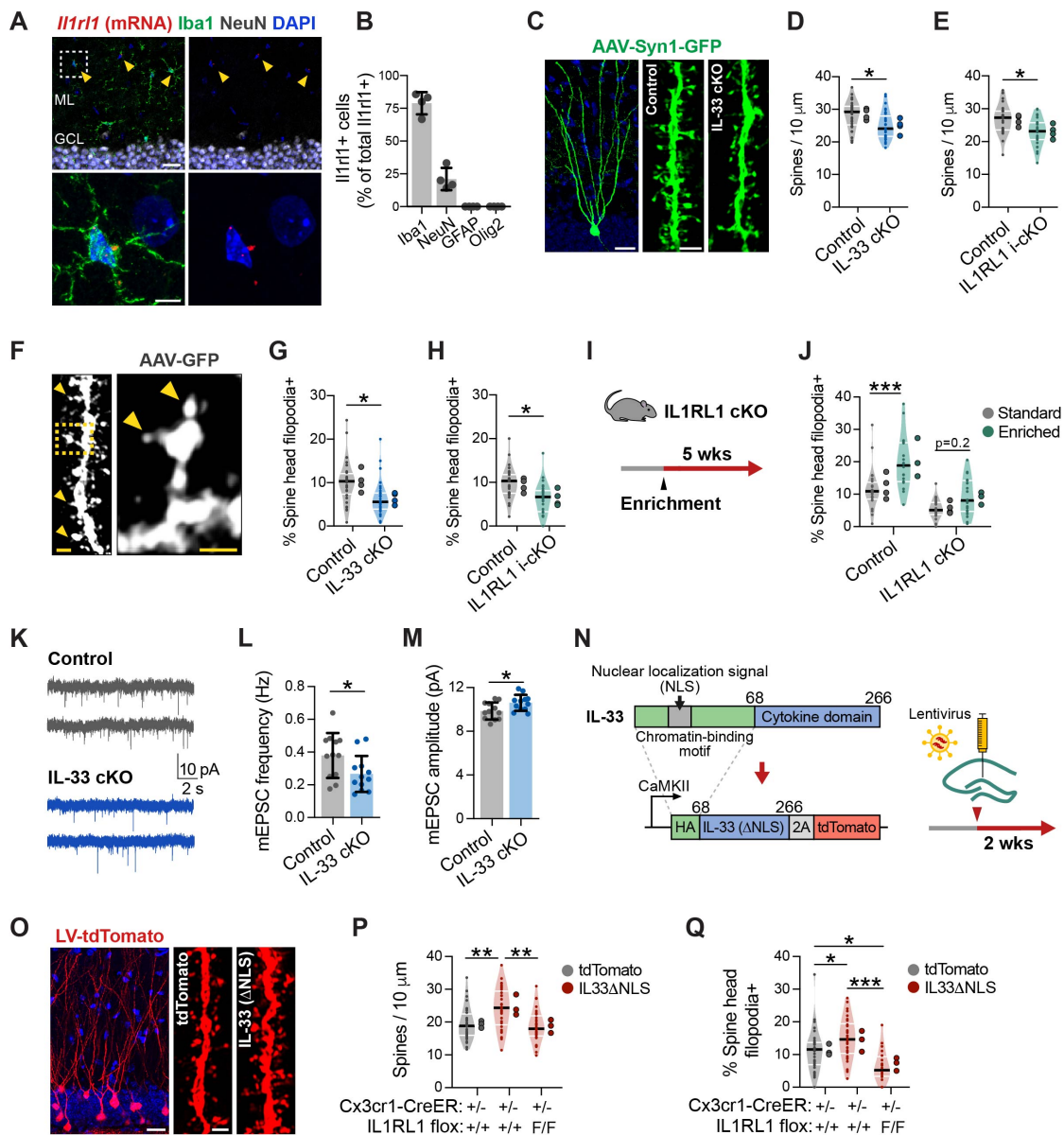
Figure 4.1: IL-33 drives experience-dependent spine plasticity.

(A-B) Representative image of *Il1rl1* transcript co-labeled with antibodies to cell-type specific markers in the DG and quantification of *Il1rl1+* cells (n = 4 mice). Scale: 25 μm, 5 μm (inset).
(C) Representative image of DG granule cells and dendritic spines in adult mice sparsely labeled with AAV$_9$-Synapsin1-GFP. AAV was injected intracerebroventricularly at P2. Scale bar: 20 μm, 2 μm (spine inset).
(D) Dendritic spine density of DG granule cells in IL-33 cKO mice vs. littermate controls (nested t-test, n = 36 dendritic segments, 4 mice/genotype).
(E) Dendritic spine density in IL1RL1 i-cKO mice vs. littermate controls (nested t-test, n = 27 dendritic segments, 4 mice/genotype).

(F) Representative image of spine head filopodia (arrowheads). Scale bar: 1 μm, 0.5 μm (inset).

(G-H) Percentage of dendritic spines harboring spine head filopodia in IL-33 cKO and IL1RL1 i-cKO vs. littermate controls (sample sizes and statistics as in D-E).

(I-J) Percent of dendritic spines with spine head filopodia in control or environmentally enriched conditions in IL1RL1 cKO mice vs. littermate controls (2-way ANOVA, Tukey's post-hoc test, n = 18-24 dendritic segments from 3-4 mice/condition)

(K) Representative traces of miniature excitatory post synaptic currents (mEPSCs) from DG granule cells in IL-33 cKO mice and littermate controls.

(L-M) Frequency and amplitude of mEPSCs from IL-33 cKO mice and littermate controls (t-test, n = 12 neurons from 3-4 mice per genotype).

(N) Schematic of IL33 NLS gain-of-function strategy. The chromatin-binding motif of mouse IL-33 was replaced by an HA epitope tag and delivered by lentiviral injection 2 weeks prior to termination.

(O-P) Representative images of dendritic segments after injection of control (tdTomato) or IL33 NLS virus. Quantification of spine density in control or IL1RL1 i-cKO mice (One-way ANOVA, Tukey's post-hoc test, n = 29-33 dendritic segments from 3 mice/group). Scale bar: 20 μm, 1 μm (inset).

(Q) Quantification of the percentage of spines harboring spine head filopodia (sample sizes and statistics as in P).

*p < 0.05, **p < 0.01, ***p < 0.001. Data represented as mean $\pm$ standard deviation for bar graphs and median $\pm$ interquartile range for violin plots. Larger dots to the right of violin plots represent the average per individual mouse within that group.
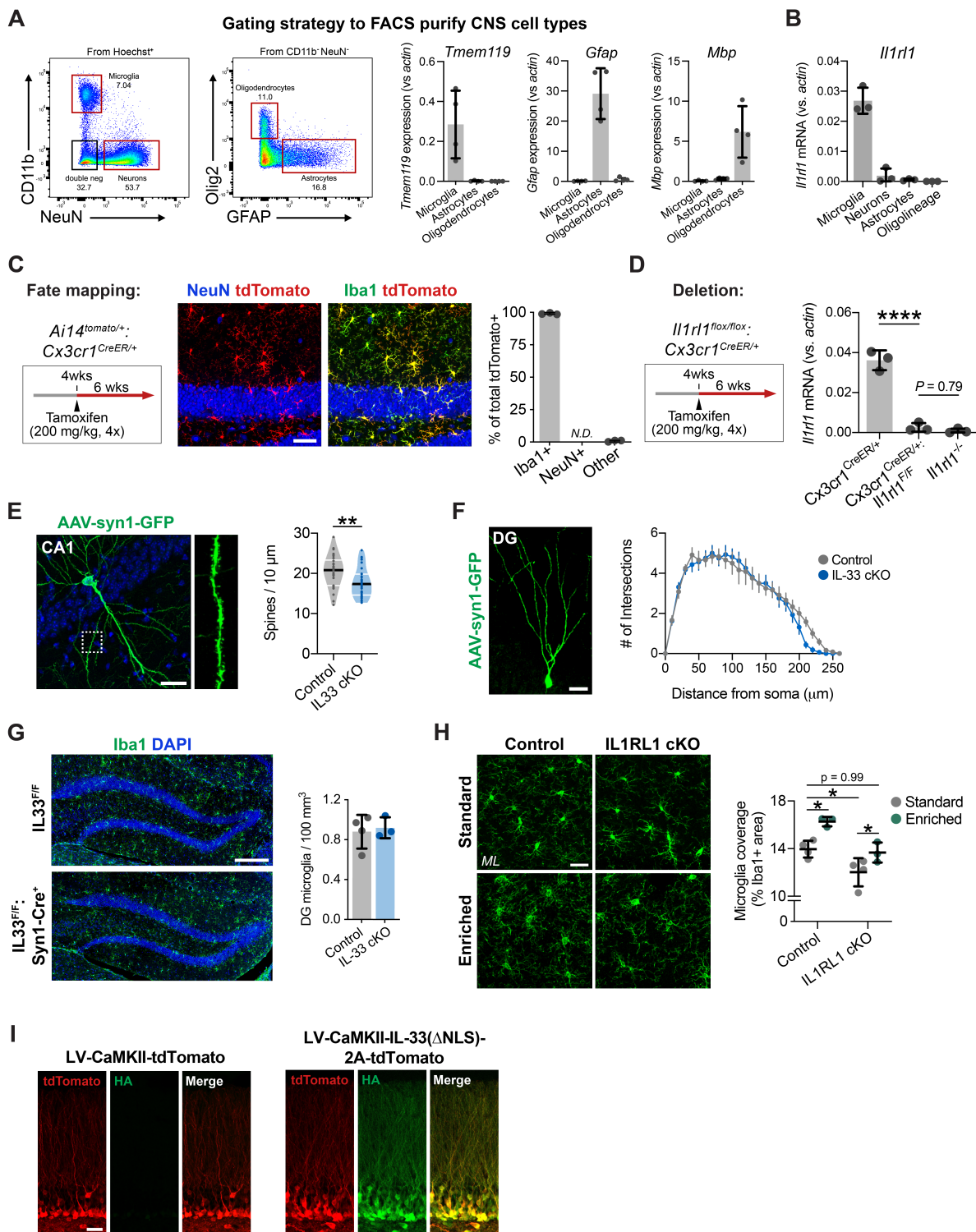
Figure 4.2: IL1RL1 expression by microglia.
(A) Gating strategy for isolation of hippocampal microglia (CD11b), neurons (NeuN), astrocytes (GFAP), and oligodendrocytes (Olig2) by FACS and expression of cell-type specific markers by qPCR (n = 4 mice).

(B) Expression of *Il1rl1* transcript in neurons and glia by qPCR of flow sorted hippocampal cell types (n = 3 mice).

(C) Schematic and representative image of *Il1rl1* excision specificity in the hippocampus using the *Cx3cr1^{creER}* allele fate mapped with the inducible Rosa26-tdTomato reporter (Ai14) and immunostaining with Iba1 and NeuN (n = 3 mice). Scale bar: 50 μm.

(D) Sensitivity of *Il1rl1* excision by qPCR of flow sorted microglia using IL1RL1 i-cKO mice (*Cr3cr1$^{CreER/+}$:Il1rl1$^{flox/flox}$* ; one-way ANOVA; Tukey's post-hoc test, n = 3 mice/group).

(E) Representative image of CA1 pyramidal neuron and quantification of dendritic spine density after loss of neuronal IL-33 (t-test, n = 30-34 dendritic segments, 3 mice/genotype). Scale bar: 20 μm.

(F) Scholl analysis of dendritic branching in DG granule cells after loss of neuronal IL-33 (t-test, Holm-Sidak multiple comparisons; n = 12-16 neurons, 3 mice). Scale bar: 20 μm.

(G) Number of Iba1+ microglia in the DG of IL-33 cKO and control mice (t-test, n = 3-4 mice). Scale bar: 200 μm.

(H) Representative images of Iba1+ microglia from control and IL1RL1 cKO mice housed under standard or enriched conditions (4 weeks). Quantification of the percentage of Iba1+ pixels (microglia coverage) in the molecular layer of the DG (one-way ANOVA, Tukey's post-hoc test, n = 3-4 mice/group). Scale bar: 20 μm.

(I) Representative image of HA epitope tag immunostaining after viral transduction with control (tdTomato) or IL-33 gain-of-function (IL-33 NLS) constructs. Scale bar: 20 μm.

*p<0.05, **p<0.01, ***p<0.001. Data = mean $\pm$ standard deviation (bar graphs) and median $\pm$ interquartile range (violin plots).

Chapter 5: Neuron-microglia signaling through IL-33 promotes experience-dependent increases in newborn neurons and is required for remote memory precision.

Integration of newborn neurons into existing circuits in the DG requires circuit remodeling and is increased in enriched environments, suggesting that this process is regulated by experience (Bergami et al., 2015; Kheirbek et al., 2012; Tashiro et al., 2006; Toni et al., 2007). We tested whether neuron-microglia signaling via IL-33 impacts newborn neurons by pulse-chase labeling with BrdU and quantification of label-retaining NeuN+ neurons 5 weeks later (**Fig. 5.1A; Fig. 5.2A**). While there was no difference in the number of newborn neurons in IL-33 cKO mice at baseline, mice housed in an enriched environment for 5 weeks had significantly fewer newborn neurons compared to controls (**Fig. 5.1B**). We did not detect differences in the number of Ki67+ proliferating cells in the subgranular zone (**Fig. 5.1C**), or alterations in the Nestin+ pool at baseline (**Fig. 5.2B**). Additionally, we found reduced dendritic spine density in newborn neurons of *Il33*$^{-/-}$ mice (**Fig. 5.2B**), indicating that synaptic integration of newborn neurons might be delayed or impaired. Taken together, these results indicate that neuronal IL-33 is required for experience-dependent increases in newborn neurons.

The decreased number of newborn neurons and impaired spine plasticity prompted us to investigate whether the IL-33 pathway is involved in hippocampal dependent memory. The DG is critical for pattern separation, a process that separates similar experiences into non-overlapping representations in the hippocampus (Miller and

Sahay, 2019). Synaptic plasticity in mature granule cells plays an important role in this process (McHugh et al., 2007; Sun et al., 2020) as does newborn neuron function (Danielson et al.; Kheirbek et al., 2012; McAvoy et al., 2016; Nakashiba et al., 2012; Sahay et al., 2011). We used a contextual fear discrimination assay to assess memory and pattern separation. Mice were conditioned to a context with 3 footshocks ('context A') and then exposed to the conditioned context followed by an unconditioned, but partially similar context B. We then quantified their ability to discriminate the two contexts at 1, 14, and 28 days post-training (**Fig. 5.1D**; McAvoy et al., 2016). We first tested animals with neuronal deletion of *Il33*, which preferentially targeted the hippocampus and prefrontal cortex, as neuronal IL-33 was not detected in other regions relevant to contextual fear memory, including entorhinal cortex, amygdala, or the nucleus reuniens (**Fig. 2.2E**; (Josselyn and Tonegawa, 2020; Ramanathan et al., 2018)).

Immediately after training, IL-33 cKO animals had intact learning and context discrimination relative to littermate controls (**Fig. 5.1E**). However, we observed a progressive decrement in the ability of IL-33 cKO mice to discriminate contexts emerging between 14- and 28-days post-training (**Fig. 5.1F-G**). This was largely driven by an increase in freezing behavior in the unconditioned context, suggesting overgeneralization of the fear memory. These deficits in contextual fear discrimination were phenocopied in animals with constitutive deletion of *Il1rl1* in microglia (**Fig. 5.1H-J**). We did not detect differences in anxiety-related behaviors in the open field or elevated plus maze tests in either IL-33 cKO or IL1RL1 cKO cohorts compared to controls (**Fig. 5.2D-G**). Collectively, our observations indicate that neuron-microglia communication through IL-33 is required

for memory precision at remote time points, suggesting a role in memory consolidation.
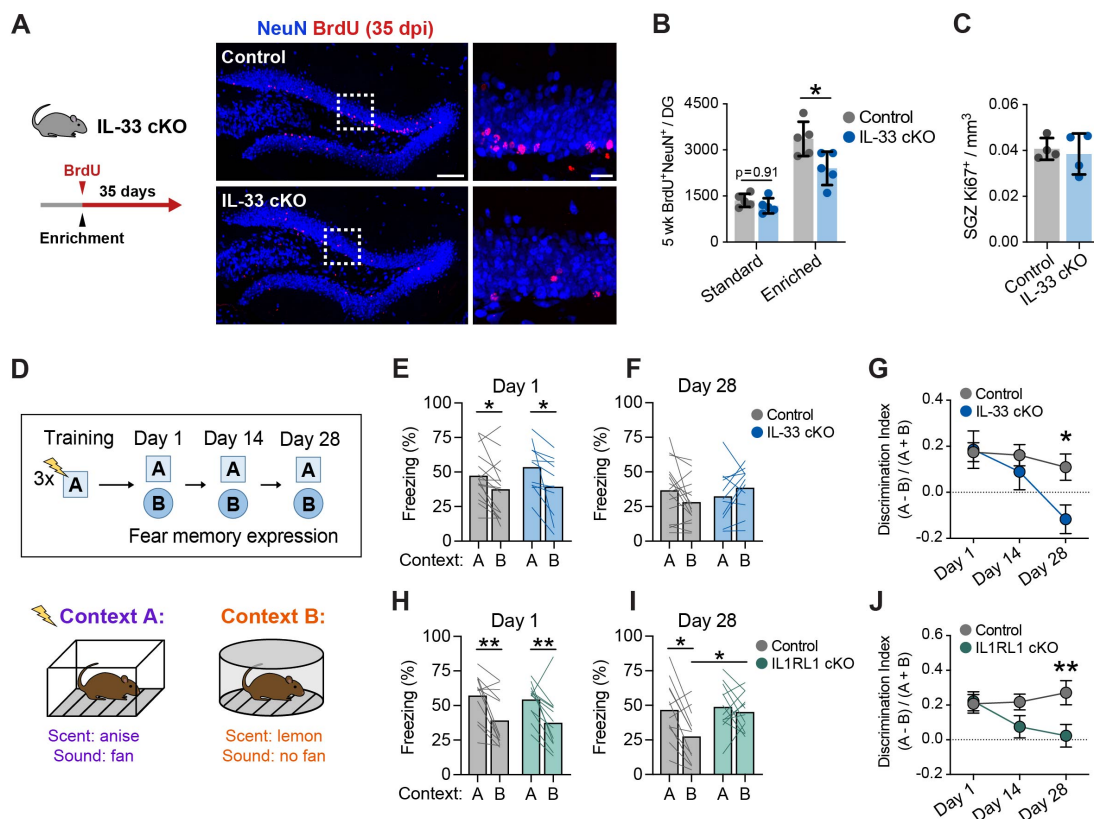
Figure 5.1: IL-33 promotes neurogenesis and memory precision.

(A-B) Representative image and quantification of 5-week old BrdU label-retaining neurons in IL-33 cKO vs. controls in standard or enriched housing (2-way ANOVA, Tukey's post-hoc test, n = 5 mice/genotype/group). Scale bar: 100 μm, 20 μm (inset).
(C) Ki67+ proliferating progenitors in the subgranular zone (SGZ) two days after enrichment (n = 3 mice/genotype).
(D) Schematic of contextual fear conditioning and context discrimination assay.
(E-G) Quantification of freezing in the conditioned fear context A vs. unconditioned context B in control and IL-33 cKO animals 1 or 28 days after training. **G** shows the same data quantified as a memory discrimination index and includes a 14-day time point (Statistics: 16 control and 11 IL-33 cKO mice, 2-way RM ANOVA with Sidak's post hoc tests. Day 1: Context: $F_{(1, 25)}$ = 15.52, p < 0.0006, Genotype: $F_{(1, 25)}$ = 0.34, p = 0.57, Interaction: $F_{(1, 25)}$ = 0.50, p = 0.49; Day 28: Context: $F_{(1, 25)}$ = 0.12, p = 0.73, Genotype: $F_{(1, 25)}$ = 0.23, p = 0.63, Interaction: $F_{(1, 25)}$ = 5.19, p = 0.03; Discrimination Index: Day: $F_{(2, 50)}$ = 4.52, p = 0.02, Genotype: $F_{(1, 25)}$ = 2.62, p = 0.12, Interaction: $F_{(2, 50)}$ = 2.61, p = 0.08).
(H-J) Quantification of freezing in context A vs. context B in control and IL1RL1 cKO animals 1 or 28 days after training. **J** shows the memory discrimination index (Statistics: 12 mice per genotype, 2-way RM ANOVA with Sidak's post hoc tests. Day 1: Context: $F_{(1, 22)}$ = 24.10, p < 0.0001, Genotype: $F_{(1, 22)}$ = 0.14, p = 0.71, Interaction: $F_{(1, 22)}$ =

0.032, p = 0.86; Day 28: Context: F(1, 22) = 9.21, p = 0.01, Genotype: F(1, 22) = 2.58, p = 0.12, Interaction: F(1, 22) = 4.27, p = 0.05; Discrimination Index: Day: F(2, 44) = 0.67, p = 0.51, Genotype: F(1, 22) = 7.51, P = 0.01, Interaction: F(2, 44) = 3.45, p = 0.04).

C

IL-33 cKO, related to Fig. 4E-G

2-way RM ANOVA Table		F(DFn, DFd)	p value
Day 1	Context	F(1, 25) = 15.52	p < 0.0006
	Genotype	F(1, 25) = 0.34	p = 0.57
	Interaction	F(1, 25) = 0.50	p = 0.49
Day 28	Context	F(1, 25) = 0.12	p = 0.73
	Genotype	F(1, 25) = 0.23	p = 0.63
	Interaction	F(1, 25) = 5.19	p = 0.03
Discrimination Index	Day	F(2, 50) = 4.52	p = 0.02
	Genotype	F(1, 25) = 2.62	p = 0.12
	Interaction	F(2, 50) = 2.61	p = 0.08

D

IL1RL1 cKO, related to Fig. 4H-J

2-way RM ANOVA Table		F(DFn, DFd)	p value
Day 1	Context	F(1, 22) = 24.10	p < 0.0001
	Genotype	F(1, 22) = 0.14	p = 0.71
	Interaction	F(1, 22) = 0.032	p = 0.86
Day 28	Context	F(1, 22) = 9.21	p = 0.01
	Genotype	F(1, 22) = 2.58	p = 0.12
	Interaction	F(1, 22) = 4.27	p = 0.05
Discrimination Index	Day	F(2, 44) = 0.67	p = 0.51
	Genotype	F(1, 22) = 7.51	p = 0.01
	Interaction	F(2, 44) = 3.45	p = 0.04

Figure 5.2: IL-33 is necessary for newborn neuron maturation.
(A) Representative image of BrdU labeled neurons 35 days post-injection and quantification of the percentage of BrdU+ label-retaining cells that are NeuN+ in IL-33 cKO and control mice (t-test, n = 5 mice/genotype). Scale bar: 20 μm.
(B) Dendritic spine density in 4-week old newborn neurons labeled with MMLV-GFP retrovirus, which selectively targets proliferating cells, in IL-33 KO and control animals (t-test, n = 34-53 dendritic segments, 3 mice). Scale bar: 20 μm, 2 μm (inset).
(C) Statistics for contextual fear discrimination assay in IL-33 cKO mice vs controls (related to Fig. 4E-G)
(D) Statistics for contextual fear discrimination assay in IL1RL1 cKO mice vs controls (related to Fig. 4H-J)

(E-F) Open field and Elevated plus maze testing of IL-33 cKO mice vs controls (t-test, n = 16 control mice, 11 IL-33 cKO mice).

(G-H) Open field and Elevated plus maze testing of IL1RL1 cKO mice (t-test, n = 12 mice/genotype).

*p < 0.05. Data = mean ± SD.

Chapter 6: IL-33 expression decreases in the aged hippocampus and is associated with decreased memory precision and spine plasticity

Altogether, our results indicate that neuron-microglia interactions via IL-33 signaling are required for proper spine plasticity and memory consolidation. Decreased synaptic plasticity and memory impairment are among the phenotypes associated with physiological aging (Segel et al., 2019; Wyss-Coray, 2016), leading us to investigate whether this pathway might be modulated with age. We observed a significant decline in the number of Il33-mCherry+ neurons in both the DG and CA1 in the hippocampus of 18-month-old mice (**Fig. 6.1A-E; Fig. 6.2A**). To determine whether physiological aging might impact memory, we quantified contextual fear learning and memory precision in young (3-month-old) vs. aged (18-month-old) mice, using the same fear conditioning paradigm as in **Fig. 5.1**. We found that after training, aged mice recognized the conditioned context A similarly to young mice. However, aged mice showed impaired context discrimination, and overgeneralization to the unconditioned context B relative to young mice (**Fig. 6.1F-G; Fig. 6.2B**). The motor response to the shock did not differ between young and old mice, suggesting that differences in freezing were not a result of altered shock sensitivity (**Fig. 6.2C**). Thus, like IL-33 cKO mice, aged mice showed reduced memory precision and increased generalization, although this discrimination deficit was already evident one day post training and persisted at a remote time point (14 days; **Fig. 6.1G**). Discrimination in this memory task tended to correlate with *Il33* mRNA levels in DG granule cells (Pearson's r = 0.47, p = 0.07, n = 11 mice; **Fig. 6.2D**).

These data suggested the possibility that at least some features of cognitive aging could be impacted by augmenting IL-33 signaling. Increased dendritic spine plasticity and neuronal activity are associated with improved cognition in the aged brain (Cai et al., 2016; Villeda et al., 2014) and in mouse models of Alzheimer's Disease (Roy et al., 2016). To test the impact of IL-33 on dendritic spines in the aged brain we used the lentiviral gain-of-function approach described in **Fig. 4.1**. We observed that aging was associated with a substantial decrease in the number of spines with spine head filopodia, and that IL-33 gain-of-function in aged mice increased the number of spine head filopodia to levels observed in young mice (**Fig. 6.1H-I**). This increase was at least partly driven by a supraphysiological increase in total spines (**Fig. 6.1J**), which were not significantly decreased with age consistent with findings by other groups (Fan et al., 2017). Physiological aging is also associated with decreased neuronal excitability (Oh et al., 2010) and age-related deficits in cognitive flexibility can be ameliorated by increasing neuronal excitability and activation (Cai et al., 2016; Villeda et al., 2014). Consistent with prior studies, we found that neuronal activation decreased with age in the DG, as measured by the percent of neurons that were c-Fos+ after exposure to a novel environment (**Fig. 6.1K-M**). IL-33 gain of function did not impact neuronal c-Fos expression in young mice but was sufficient to increase the number of c-Fos+ neurons in old mice to the levels observed in young mice (**Fig. 6.1M**). These data suggest that aging is a physiologic context associated with decreased *Il33* expression and impaired memory precision and that increasing neuronal IL-33 release in individual neurons improves some structural and functional correlates of brain aging.
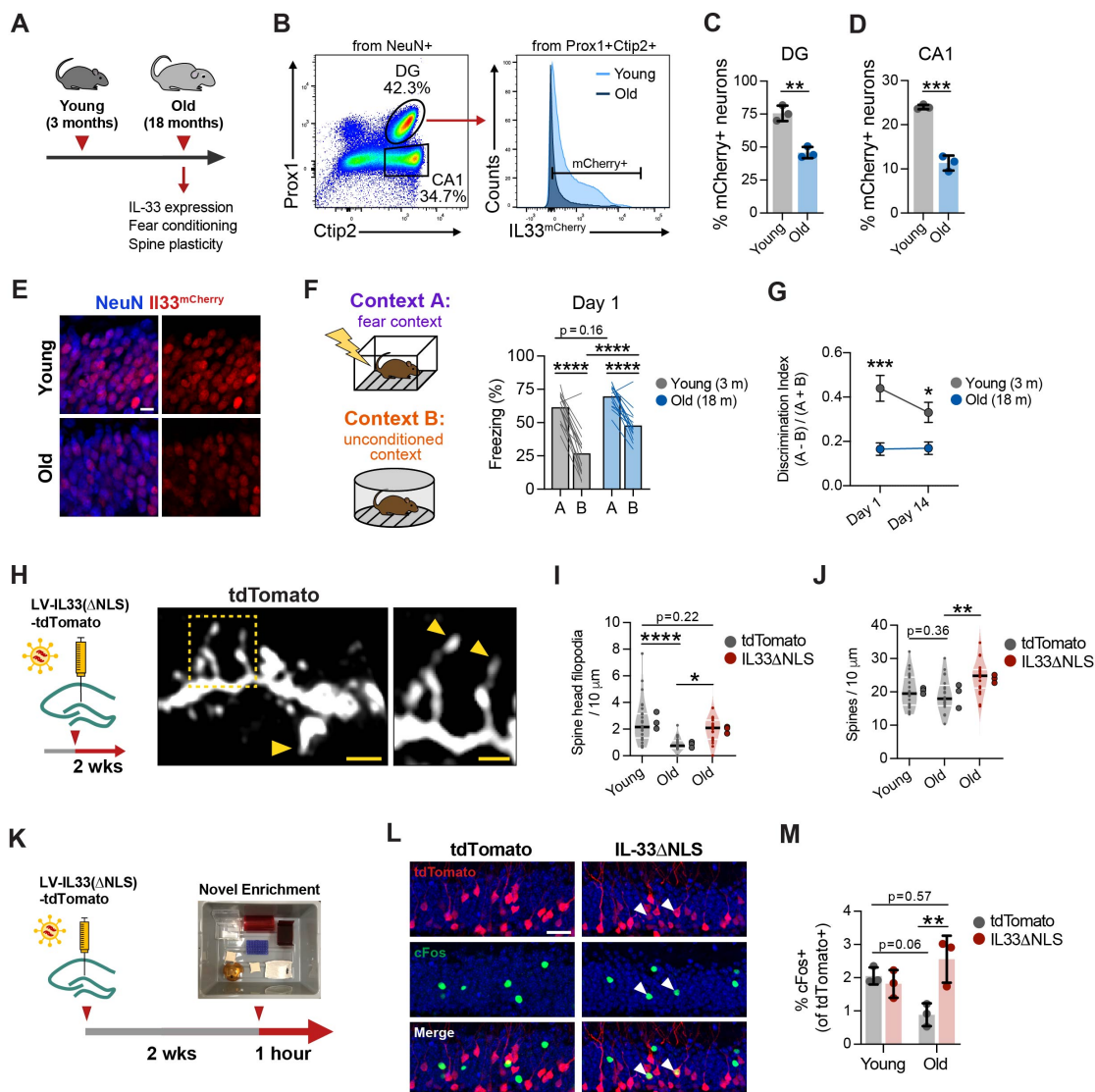
Figure 6.1: Age-related IL-33 expression and memory precision.

(A) Schematic of experimental design.

(B-D) Representative gating of mCherry+ neurons and quantification of *Il33* expression in the DG and CA1 of young and aged mice (t-test, 3 mice/group).

(E) Representative image of Il33-mCherry in the DG of young and old *Il33^{mCherry/+}* mice. Scale bar: 10 μm.

(F) Schematic of the contextual fear discrimination assay performed in Figure 4 and quantification of freezing in context A vs context B one day post-training in young (3 month) and old (18 month) mice (16 young mice and 14 old mice, 2-way RM ANOVA with Sidak's post hoc tests. Context: $F_{(1, 28)} = 107.7$, $p < 0.0001$, Age: $F_{(1, 28)} = 15.44$, $p = 0.0005$, Interaction: $F_{(1, 28)} = 5.669$, $p = 0.02$).

(G) Discrimination indices at days 1 and 14 post-training in young and old mice. (16 young mice and 14 old mice, 2-way RM ANOVA with Sidak's post hoc tests. Day: $F_{(1, 28)} = 3.637$, $p = 0.06$, Age: $F_{(1, 28)} = 14.41$, $p = 0.0007$, Interaction: $F_{(1, 28)} = 1.726$, $p = 0.19$).
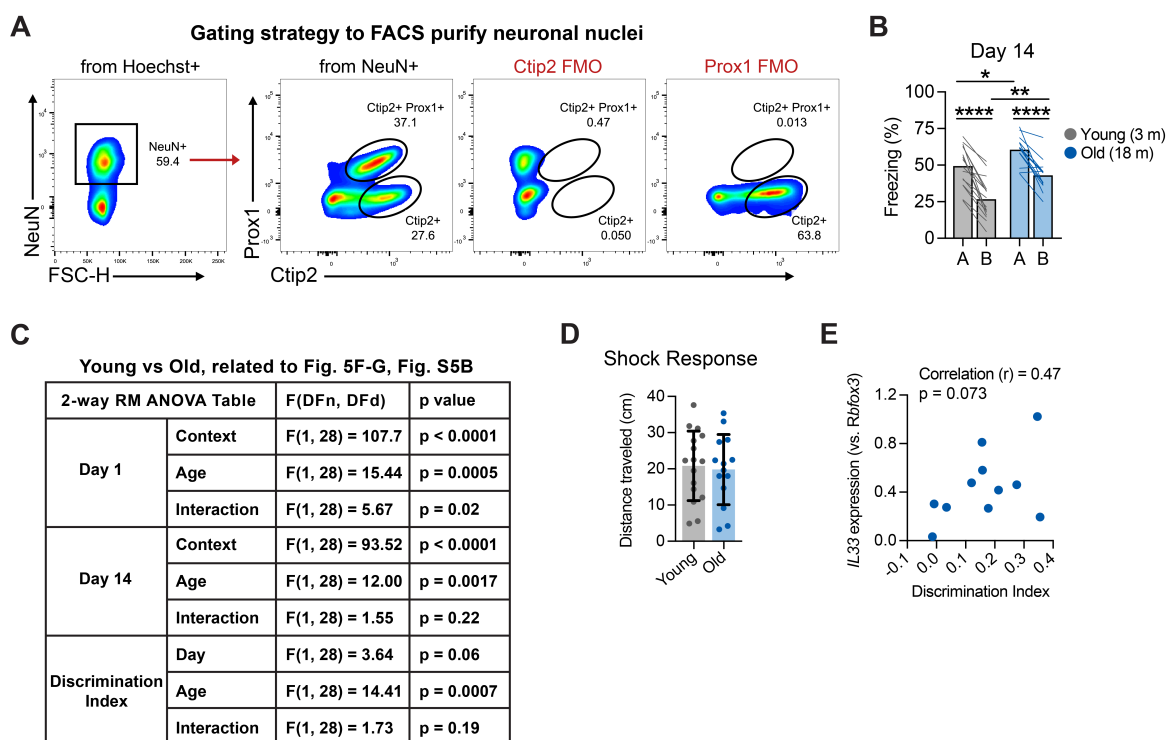
(H-J) Representative image and quantification of spine head filopodia (**I**) and total spines (**J**) in young and old mice after injections with control or IL-33 gain-of-function virus (One-way ANOVA, Tukey's post-hoc test, n = 20-27 dendritic segments, 3 animals/group). Scale bar: 2 μm, 1 μm (inset).

(K) Schematic to measure neuronal activation in young and old mice. Two weeks after injections with control or IL33 NLS virus, mice were exposed to a novel environment for 1 hour.

(L-M) Representative image and quantification of percent of virally labeled DG neurons that were cFos+ following 1 hour of novel environment (One-way ANOVA, Tukey's post-hoc test, 3 mice/group). Scale bar: 20 μm.

*p < 0.05, **p < 0.01, ****p < 0.0001. Data represented as mean ± standard deviation for bar graphs and median ± interquartile range for violin plots. Larger dots to the right of violin plots represent the average per individual mouse within that group.

C Young vs Old, related to Fig. 5F-G, Fig. S5B

2-way RM ANOVA Table		F(DFn, DFd)	p value
Day 1	Context	F(1, 28) = 107.7	p < 0.0001
	Age	F(1, 28) = 15.44	p = 0.0005
	Interaction	F(1, 28) = 5.67	p = 0.02
Day 14	Context	F(1, 28) = 93.52	p < 0.0001
	Age	F(1, 28) = 12.00	p = 0.0017
	Interaction	F(1, 28) = 1.55	p = 0.22
Discrimination Index	Day	F(1, 28) = 3.64	p = 0.06
	Age	F(1, 28) = 14.41	p = 0.0007
	Interaction	F(1, 28) = 1.73	p = 0.19

Figure 6.2: Validation of age-related IL-33 expression.

(A) Representative gating strategy to isolate neuronal nuclei from Prox1$^+$Ctip2$^+$ dentate granule cells and Prox1$^-$Ctip2$^+$ pyramidal neurons with fluorescence minus one (FMO) negative staining controls.

(B-C) Quantification of freezing in context A vs context B fourteen days post-training in young and old mice (n = 16 young mice and 14 old mice, 2-way RM ANOVA, Sidak's post hoc tests). Statistics for contextual fear discrimination assay in young vs old mice (also related to Fig. 5F-G).

(D) Quantification of distance traveled in young and old mice during the first 2 second footshock (t-test, n = 16 young and 14 old mice. Mean ± SD.).

(E) Correlation between day 14 discrimination index and expression of *Il33* mRNA in flow sorted dentate granule cells in individual old mice (Pearson correlation, n = 11 mice).
*p < 0.05, **p < 0.01, ***p < 0.001, ****p < 0.0001.

Chapter 7: Neuronal IL-33 drives microglial engulfment of extracellular matrix

The deficient spine numbers after loss of IL-33-IL1RL1 signaling indicated a role for IL-33 in synapse formation or maintenance and a requirement for microglia in this process. To interrogate potential mechanisms by which IL-33 impacts microglia, we transcriptionally profiled hippocampal microglia after four hours of *in vivo* exposure to IL-33 (**Fig. 7.1A; Fig. 7.2A**). As expected, we identified a strong activation signature after IL-33 treatment, including *Il1b*, *Tnf*, and multiple chemokines (**Fig. 7.1B**). Among the top upregulated genes were the class A scavenger receptor *Marco*, a regulator of filopodial morphogenesis and debris clearance (van der Laan et al., 1999; Pikkarainen et al., 1999) and the adaptor protein *Gas7*, which is necessary for phagocytic cup formation in cultured macrophages (Hanawa-Suetsugu et al., 2019). These findings are consistent with IL-33's role in promoting phagocytosis (Fu et al., 2016; Vainchtein et al., 2018).

We next investigated potential pathways relevant to the role of IL-33 in promoting spine formation. In peripheral tissues, IL-33 promotes tissue remodeling, which includes turnover of extracellular matrix (ECM; (Bonnans et al., 2014; Molofsky et al., 2015)). Live imaging studies suggest that brain ECM is dynamic and responsive to synaptic cues (Tønnesen et al., 2018), and multiple studies have shown that extracellular matrix proteins can restrict synaptic plasticity and dendritic spine remodeling. (Bolós et al., 2018; Frischknecht et al., 2009; Oray et al., 2004; Orlando et al., 2012; Pizzorusso et al., 2006; de Vivo et al., 2013). We found that 76 genes differentially expressed after IL-33 treatment

were associated with the ECM ((Naba et al., 2016); **Fig. 7.1B**, green dots). Of these, we identified 9 genes classified as ECM regulators that were significantly upregulated after IL-33 treatment (**Fig. 7.1C**). These included multiple ECM proteases, including *Adamts4*, *Mmp14*, *Mmp25*, and *Ctsc.* Some of these cleave multiple ECM substrates, whereas others (e.g. *Adamts4)* are membrane-localized metalloproteases that predominantly cleave chondroitin sulfate proteoglycans (CSPGs), which are a major class of ECM proteins in the brain (**Fig. 7.1D;** (Barbolina and Stack, 2008; Kelwick et al., 2015; Levy et al., 2014)).

Aggrecan is a CSPG highly enriched in the brain and particularly prominent in the diffuse ECM of the hippocampal DG **(Fig. 7.1D-E, Fig. 7.2B** (Bolós et al., 2018; Rowlands et al., 2018)). We therefore investigated whether microglia can engulf Aggrecan. Using superresolution imaging and 3D reconstructions, we identified Aggrecan immunostaining within microglia and found that it localized within CD68+ lysosomes (**Fig. 7.1F**). In microglia from IL-33 cKO mice, we found decreased numbers of CD68+ lysosomes compared to controls, indicating that IL-33 promotes a phagocytic phenotype (**Fig. 7.1G-H**). Additionally, we also found a 54% reduction in the amount of engulfed Aggrecan in microglia from IL-33 cKO mice compared to controls (**Fig. 7.1I**). In contrast, IL-33 gain-of-function was sufficient to increase microglial process coverage, phagocytic index, and engulfment of Aggrecan (**Fig. 7.1J-K, Fig. 7.2D-F**). In summary, we show that neuron-derived IL-33 promotes microglial phagocytosis and engulfment of the CSPG Aggrecan.
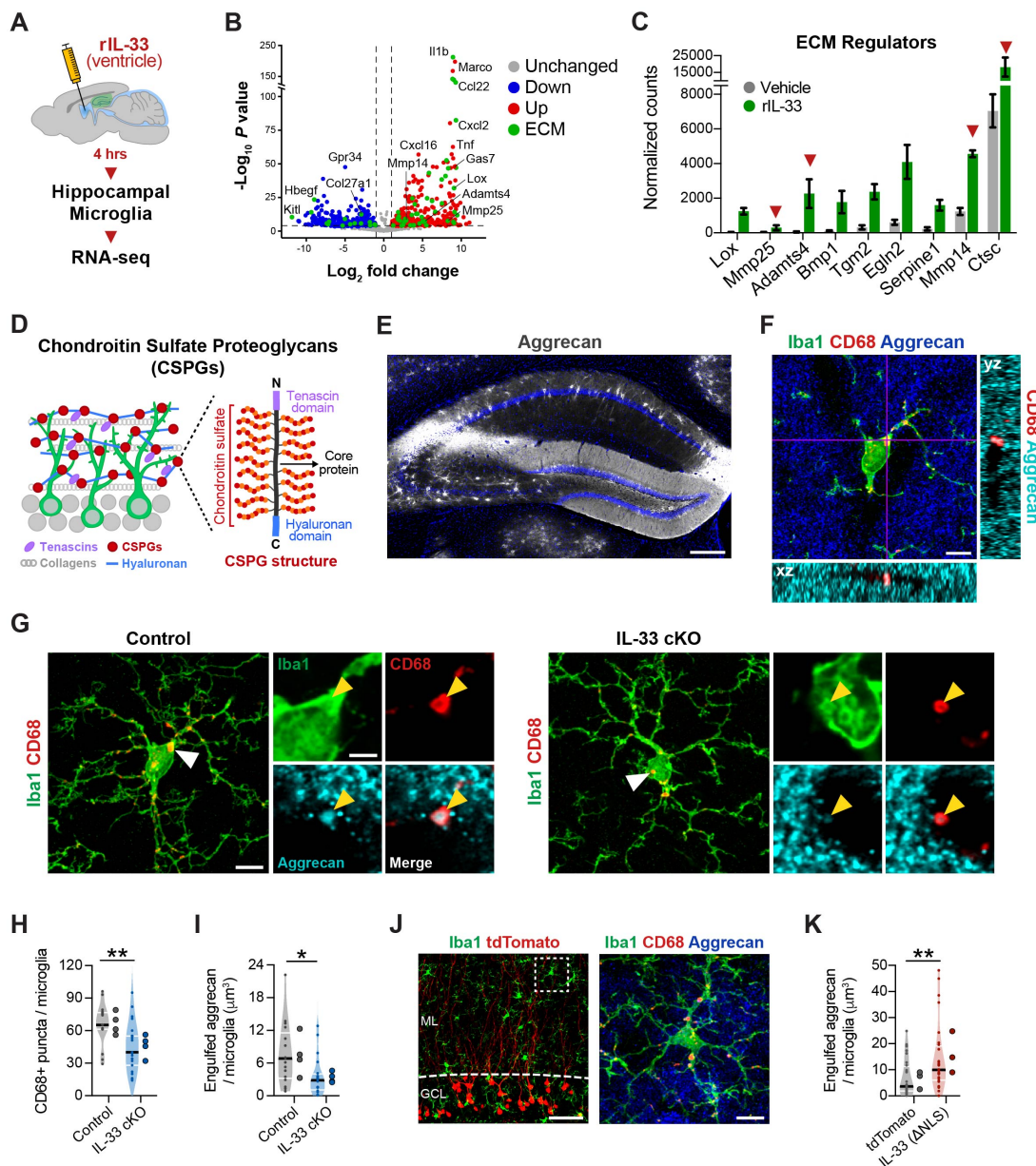
Figure 7.1: Neuronal IL-33 drives microglial engulfment of extracellular matrix.

(A) Recombinant IL-33 was injected intracerebroventricularly and microglia were isolated by FACS 4 hours later for transcriptional profiling.

(B) Volcano plot of differentially expressed genes between IL-33 and PBS treated mice (adjusted p-value < 0.01, see Methods). Green dots highlight ECM and ECM-interacting genes from the Matrisome database (Naba et al., 2016).

(C) Significantly upregulated genes from (**B**) classified as ECM regulators (Naba et al., 2016). Red arrows: ECM proteases.

(D) Schematic of extracellular matrix in the DG and structure of chondroitin sulfate proteoglycans (CSPGs).

(E) Representative image of Aggrecan in the hippocampus. Scale bar: 250 μm.

(F) Z-stack and cross-sectional view of Iba1+ microglia with engulfed Aggrecan within CD68+ lysosomes in the DG. Scale bar: 5 μm.

(G-I) Representative images and quantification of CD68+ lysosomes within microglia **(H)** and Aggrecan protein within microglial lysosomes **(I)** (t-test, n = 17-20 microglia, 4 mice/genotype). Scale bar: 5 μm, 2 μm (inset).

(J-K) Representative image and quantification of Aggrecan engulfment in microglia 2 weeks after viral infection with control or IL-33 NLS virus in the DG (t-test, 28 microglia, 3 mice/group). Scale bar: 25 μm, 2 μm (inset).

*p < 0.05, **p < 0.01, ****p < 0.0001. Data represented as mean ± standard deviation for bar graphs and median ± interquartile range for violin plots. Larger dots to the right of violin plots represent the average per individual mouse within that group.
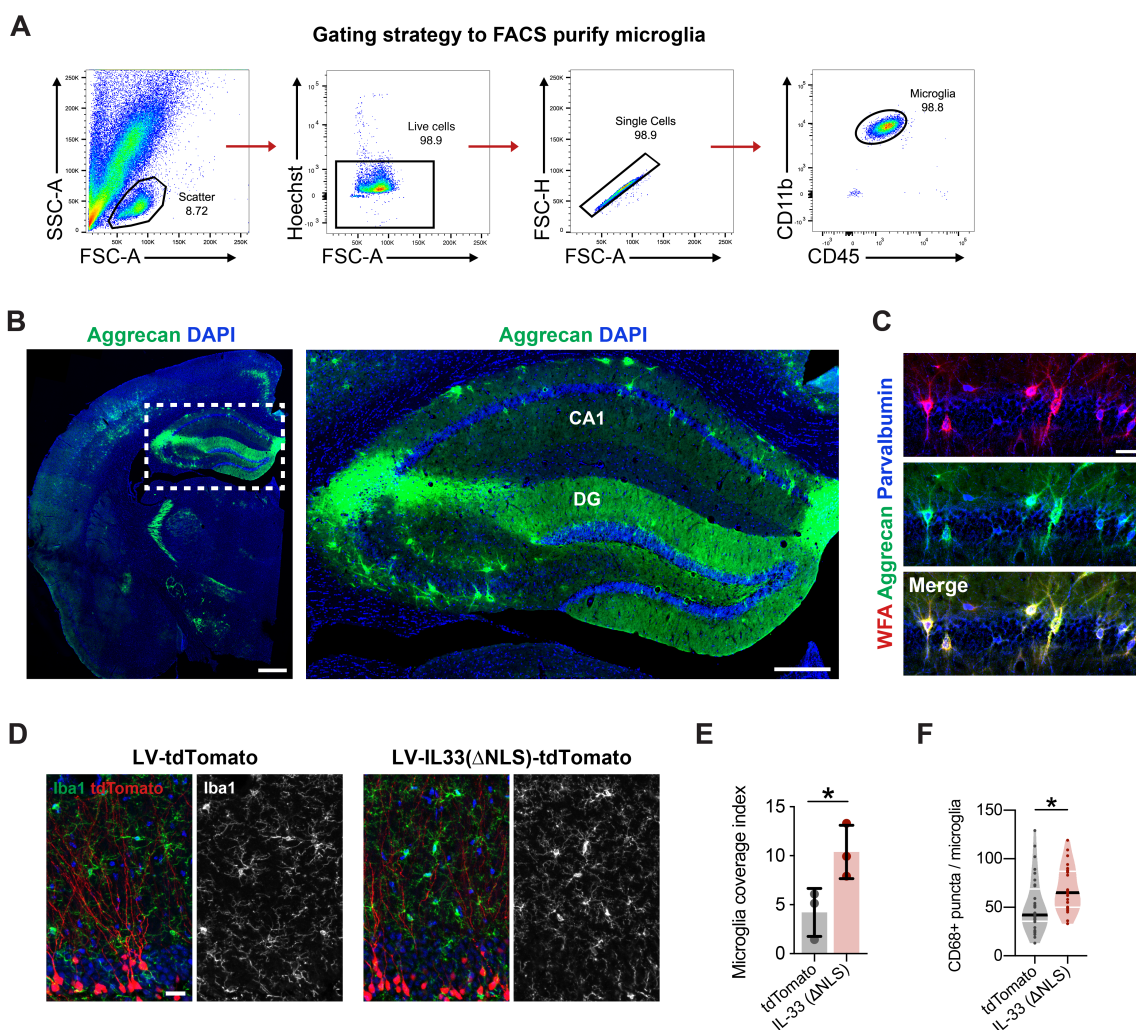
Figure 7.2: Extracellular matrix in the brain
(A) Representative gating strategy to isolate live microglia (CD11b+CD45+).

(B) Representative hemisection from adult (P90) mouse showing Aggrecan immunostaining. Inset = hippocampus. Scale bar: 500 μm, 250 μm (inset).

(C) Aggrecan colocalization with WFA+ perineuronal nets around Parvalbumin+ interneurons in CA1. Scale bar: 50 μm.

(D-E) Representative image and quantification of microglial process coverage index calculated as the percentage of Iba1+ pixels in a field of view normalized to the percentage of tdTomato+ pixels after viral transduction with control or IL-33 NLS constructs (t-test, n = 3 mice). Scale bar: 20 μm.

(F) Quantification of number of CD68+ lysosomes in microglia after viral transduction with control or IL-33 NLS constructs (t-test, 28 microglia, 3 mice/group).

*p<0.05. Data = mean $\pm$ standard deviation (bar graph) and median $\pm$ interquartile range (violin plot).

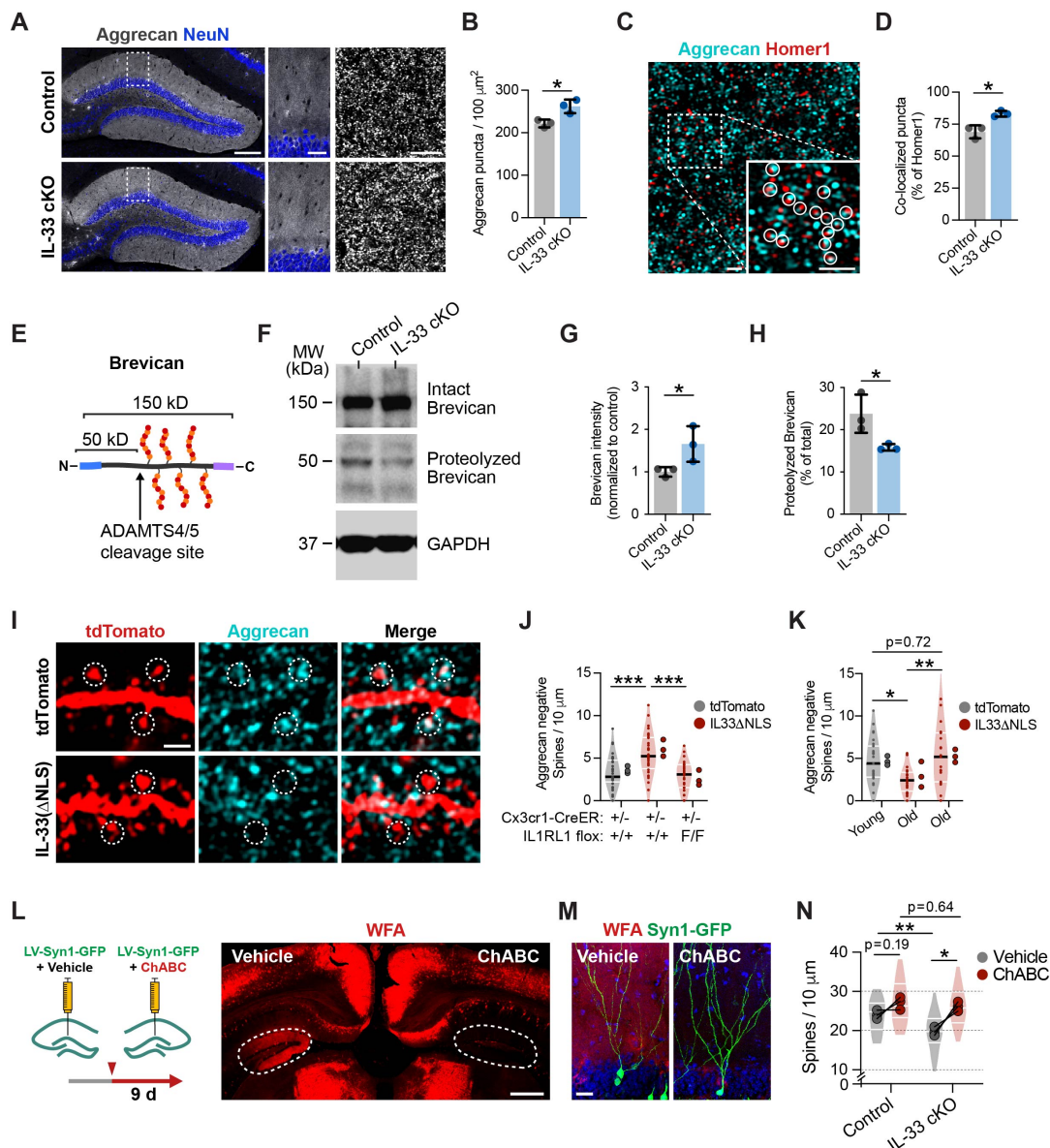# Chapter 8: IL-33 deficiency leads to accumulation of perisynaptic ECM

To determine if microglial remodeling of the ECM could impact accumulation of ECM near synapses, we used anti-Aggrecan antibodies to quantify Aggrecan in the hippocampi of IL-33 cKO mice. Using superresolution imaging, we found that Aggrecan in the DG molecular layer formed punctate structures that colocalized with the postsynaptic density protein Homer1. IL-33 cKO mice had a significant increase in the density of Aggrecan deposition compared to littermate controls, as well as increased colocalization of Aggrecan with Homer1 (**Fig. 8.1A-D**). Brevican is another CSPG prevalent in the adult brain that can restrict synaptic plasticity (Favuzzi et al., 2017; Frischknecht et al., 2009) and is proteolytically cleaved into a smaller 53 kDa fragment by the metalloprotease ADAMTS4 (Mayer et al., 2005; Valenzuela et al., 2014); **Fig. 8.1E**). We found that loss of neuronal IL-33 led to a 66% increase in total Brevican and a 34% decrease in the levels of proteolyzed Brevican compared to control mice (**Fig. 8.1F-G**).

We next used our IL-33 gain of function approach to further examine the relationship between Aggrecan and dendritic spines. We found that approximately 85% of dendritic spines in young adult animals were in close proximity to Aggrecan+ puncta (Fig. 8.1**I**). IL-33 gain-of-function increased the number of spines devoid of Aggrecan contact and this effect required microglial expression of the IL-33 receptor IL1RL1 (**Fig. 8.1J**). In aged animals, we found a two-fold decrease in the number of spines devoid of perisynaptic Aggrecan, consistent with studies that have found marked accumulation of ECM proteins with age (Végh et al., 2014a). We found that IL-33 gain-of-function

increased the number of Aggrecan negative spines to levels seen in young mice (**Fig. 8.1K**). These data indicate that IL-33 promotes ECM remodeling and restricts ECM deposition near synapses.

Finally, we sought to determine the relationship between IL-33's impact on the ECM and its role in promoting dendritic spine maintenance. We injected the enzyme Chondroitinase ABC (ChABC) into the DG, which compromises ECM integrity by degrading the glycosaminoglycan side chains present on CSPGs (**Fig. 8.1L**). We found that 9 days after ChABC injection, spine density was modestly increased in controls (p = 0.19), but was significantly increased in IL-33 cKO mice to the levels of ChABC-treated controls (**Fig. 8.1M-N**). These data support the hypothesis that IL-33's effects on spines are mediated, at least in part, through its impact on the ECM, and taken together, directly implicate microglia as regulators of ECM clearance and spine formation.

Figure 8.1 IL-33 deficiency leads to accumulation of perisynaptic ECM.

(A) Immunostaining of Aggrecan deposition in the DG in control and IL-33 cKO mice. Insets shows higher magnification view of Aggrecan in the molecular layer. Scale bar: 200 μm (left), 40 μm (middle), 5 μm (right).
(B) Quantification of Aggrecan puncta density (t-test, n = 3 mice/genotype).
(C-D) Representative image and quantification of Aggrecan and Homer1 immunostaining and co-localization in the molecular layer. Inset shows colocalization between Aggrecan and Homer1 (circles). Scale bar: 1 μm, 1 μm (inset) (t-test, n = 3 mice/genotype).
(E) Schematic of Brevican proteoglycan and proteolytic cleavage site.
(F-H) Representative image of western blot of Brevican from whole hippocampal lysate in IL-33 cKO and littermate controls, including uncleaved (150 kD) and cleaved (50 kD)

Brevican. Quantifications of total (**G**) and cleaved (**I**) Brevican (t-test, n = 3 mice/genotype).

(I) Representative images of Aggrecan co-localization with dendritic spines in the DG. Scale bar: 1 μm.

(J) Quantification of Aggrecan-negative dendritic spines from IL1RL1 i-cKO or littermate controls injected with control (tdTomato) or IL-33 gain of function (IL-33 NLS) virus (One-way ANOVA, Tukey's post-hoc test, n = 29-33 dendritic segments, 3 mice/group).

(K) Quantification of Aggrecan-negative dendritic spines from young and old mice injected with control (tdTomato) or IL-33 gain of function (IL-33 NLS) virus (One-way ANOVA, Tukey's post-hoc test, n = 19-27 dendritic segments, 3 mice/group).

(L-M) Schematic of Chondroitinase ABC (ChABC) injection paradigm and representative image of *wisteria floribunda* (WFA) lectin staining in the DG (dashed circles) injected bilaterally with ChABC or vehicle. Dentate granule cells in hemispheres injected with ChABC or vehicle (**M**). Scale bar: 500 μm (L), 20 μm (M).

(N) Quantification of dendritic spines in IL-33 cKO or control mice injected bilaterally with ChABC or vehicle (Two-way repeated measures ANOVA, Sidak's post-hoc test, n = 3 mice/genotype; dots represent means per mouse, lines connect vehicle and ChABC injected hemispheres; violin plots included to show distribution of dendritic segments for each group, 23-30 dendritic segments).

Chapter 9: Discussion

This study defines a cytokine-mediated mechanism that acts through microglia to promote dendritic spine plasticity and precise retrieval of remote memories. We find that neurons determine microglial responses by experience-dependent regulation of IL-33, thus coupling neuronal state to microglial activation. Finally, we demonstrate that IL-33 drives microglial engulfment of the extracellular matrix, revealing a molecular mechanism through which microglial activation leads to increases in synaptic plasticity. The instructive role of IL-33 in promoting microglial functions, and the fact that IL-33 is heterogeneously expressed by hippocampal neurons suggests two levels at which specificity can be encoded into the circuit. First, we show that environmental inputs including enrichment and social isolation can alter the set point of this homeostatic circuit by altering tonic *Il33* expression in neurons. Secondly, our data indicates that DG neurons are not all equally poised for learning. IL-33+ neurons in the DG are highly enriched for genes linked to synapse formation. Many studies have demonstrated that neuronal activity and other functional correlates can bias neuronal recruitment into a memory trace (Cai et al., 2016; Han et al., 2007; Park et al., 2016) and that some, but not all of these neurons become dissociated from this memory trace with time (Guo et al., 2018; Kitamura et al., 2017). Our work reveals candidate molecular mechanisms that might underlie this diversity and preferential engagement or retention within engram networks. Furthermore, they suggest a mechanism by which plasticity can be enhanced in enriched environments and suppressed in the context of stress and deprivation.

Microglia remodel the brain extracellular matrix

How do microglial interactions with synapses promote spine formation and plasticity? An abundance of live imaging data has shown that microglial processes constantly move within the neuropil and make contact with dendritic spines in an activity dependent manner (Eyo et al., 2014, 2015; Li et al., 2012; Madry et al., 2018; Tremblay et al., 2010; Wake et al., 2009). In the CA1 region, spine head filopodia formation is induced by perisynaptic microglia contact (Weinhard et al., 2018) and local turnover of chondroitin sulfate proteoglycans (Orlando et al., 2012). Our data raise the possibility that these frequent microglial contacts with spines could enable microglia to locally clear or modulate ECM around individual synapses in support of activity-dependent structural plasticity.

It has been proposed that memories may be stored in the 'pattern of holes' in the ECM, based on the findings that ECM restricts synaptic plasticity and that ECM proteins are extremely long-lived (Tsien, 2013). Our findings that microglia are required for memory consolidation, but not learning suggest a form of microglia-dependent plasticity that occurs on an extended timescale of days to weeks and could well impact stable changes in the brain ECM. Notably, ECM is not only relevant to synapses. For example, oligodendrocytes are abundant producers of ECM, which is required for proper assembly of nodes of Ranvier (Susuki et al., 2013). New myelin formation also promotes long-term memory precision (Pan et al., 2020; Steadman et al., 2020). This raises the question of

whether microglia could also play a role in the remodeling of myelin or other components of brain structure.

IL-33 function in physiology, aging, and pathology

Dysregulation of innate immune homeostatic mechanisms and of microglia are strongly implicated in the cognitive dysfunction that occurs in brain aging and disease (Bennett and Molofsky, 2019; Kelley et al., 2018). Our data reveal a key role for IL-33 dependent neuron-microglia signaling in experience-dependent remodeling. The progressive decline in neuronal IL-33 expression with age coincides with defects in memory precision, and an accumulation of perisynaptic ECM (Végh et al., 2014a). Interestingly, both clearance of ECM and exogenous recombinant IL-33 are beneficial in mouse models of Alzheimer's Disease (Fu et al., 2016; Végh et al., 2014b). Thus, precisely defining the molecular mechanisms that regulate microglial synaptic function in the healthy brain may lead to new tools and approaches for cognitive repair.

Materials and Methods

EXPERIMENTAL MODELS AND SUBJECT DETAILS

Mice: All mouse strains were maintained in the University of California San Francisco specific pathogen–free animal facility, and all animal protocols were approved by and in accordance with the guidelines established by the Institutional Animal Care and Use Committee and Laboratory Animal Resource Center. Littermate controls were used for all experiments when feasible, and all mice were backcrossed >10 generations on a C57Bl/6 background unless otherwise indicated.

Environmental enrichment consisted of housing 2-3-month old mice in large ventilated rat cages (210 sq. in, Lab Products) with standard nesting, rodent foraging toys, and one running wheel per cage (https://larc.ucsf.edu/rodent-enrichment). Social isolation conditions consisted of singly housing 4-week old mice immediately after weening in standard mouse cages devoid of enrichment toys.

Viral Constructs: For sparse labeling of hippocampal neurons, adeno-associated virus (AAV$_9$-hSyn1-eGFP) was packaged and supplied by the Addgene/UPENN vector core (Addgene viral prep # 105539-AAV9) at titers of ~1x10^{13} vg/mL. For IL-33 gain of function experiments, lentiviral vectors (LV-CaMKII-tdTomato and LV-CaMKII-IL33(ΔNLS)-2A-tdTomato) were designed in house and packaged by the UCSF virus core at titers of ~1x10^7 vg/mL. For labeling adultborn neurons, MMLV retrovirus vector (CAG-GFP) was supplied by Addgene (Plasmid #16664) and packaged into retrovirus by the UCSF virus

core at titers of ~1x10^6 vg/mL. LV-Synapsin-GFP lentivirus was purchased from SignaGen Laboratories.

METHOD DETAILS

Tamoxifen and BrdU injections: Tamoxifen (Sigma, T5648) was diluted in Corn Oil (Sigma-Aldrich) at 37°C overnight and administered by oral gavage at a concentration of 200 mg/kg four times every other day beginning at 4 weeks of age. For all BrdU labeling experiments, BrdU (Sigma-Aldrich) was diluted in a 10 mg/mL stock solution in sterile 1X PBS and injected intraperitoneally at a concentration of 100 mg/kg daily for 3 days.

Stereotaxic injections: All brain injections were performed with a Kopf stereotaxic apparatus (David Kopf, Tujunga, CA) with a microdispensing pump (World Precision Instruments) holding a beveled glass needle with ~50 μm outer diameter. For perinatal injections to sparsely label hippocampal neurons, P2-3 mice were anesthetized by hypothermia, headfixed with a custom clay mold, and 0.5 μl of AAV$_9$-hSyn1-eGFP was injected at a rate of 15 nL/sec into the right ventricle using in house coordinates (1.5 mm AP from lambda, 0.8 mm ML, -1.6 mm DV). A dilution of 1:250 in sterile saline was used for experiments measuring dendritic spine density and a 1:750 dilution was used for experiments requiring single neuron morphology. Mice were allowed to recover on a heat pad before being returned to their cage.

For injections into adult hippocampus, mice were anesthetized with 1.5% isoflurane at an oxygen flow rate of 1L/min, headfixed with a stereotaxic frame, and treated with ophthalmic eye ointment. Fur was shaved and the incision site was sterilized

with 70% ethanol and Betadine prior to surgical procedures. A hole was drilled in the skull and 1.5 uL of LV-CaMKII-tdTomato or LV-CaMKII-IL33(ΔNLS)-2A-tdTomato was injected at a 1:25 dilution in sterile saline (-2.1 mm AP, 1.375 mm ML, x -1.7 mm DV) at a rate of 3 nL/sec. For injections with Chondroitinase ABC (Sigma), 40 U/mL were injected with LV-Synapsin-GFP (SignaGen Laboratories) at a dilution of 1:150. Body temperature was maintained throughout surgery using a heating pad. Post-surgery, Buprenorphine (Henry Schein Animal Health) was administered as needed by intraperitoneal injection at a concentration of 0.1 mg/kg.

Immunohistochemistry and Confocal Microscopy: For all immunohistochemistry experiments, mice were perfused transcardially with ~10 mL of ice-cold 1X PBS followed by ~10 mL of 4% (weight/volume) paraformaldehyde diluted in PBS. Brains were post-fixed in 4% PFA for a minimum of 4 hours and then transferred to a 30% sucrose solution for a minimum of 2 days. Brains were then flash frozen and sliced in 40 um thick coronal sections on a HM 440E freezing microtome (GMI Instruments).

For immunohistochemistry, brain sections were incubated in a blocking solution consisting of 10% normal goat or donkey serum (Thermo Fisher) and 0.4% Triton (Sigma-Aldrich) diluted in 1X PBS. Primary antibodies were diluted in 3% normal goat or donkey serum in 0.4% Triton and tissue was incubated on a shaker overnight at 4°C. Secondary antibodies were diluted in 3% normal goat or donkey serum and tissue was incubated on a shaker for 2 hours at room temperature with Hoechst 33342 (Thermo Fisher) added at 1:5000 during the last 5 minutes of incubation. Brain sections were mounted on coverslips

with ProLong Glass without DAPI (Thermo Fisher) for high resolution imaging and ProLong Gold (Thermo Fisher) for all other experiments.

For IL-33 staining, brain sections were heated in a 1X Sodium Citrate solution (Fisher Scientific) at 95°C for 10 minutes and then washed 3x with PBS prior to blocking. For BrdU staining, brain sections were stained with non-BrdU primary antibodies and secondary antibodies as described above and then incubated with 4% PFA for 10 minutes at room temperature. Brain sections were incubated in 2N HCl (Sigma-Aldrich) for 30 minutes at 37°C and then quenched with Boric Acid buffer (0.31 g/50 mL in H_2O, pH 8.5) for 10 minutes at room temperature before being carefully washed four times with 1X PBS. Tissue was incubated in a blocking solution of 10% normal goat serum and 0.4% Triton on a shaker for 1 hour at room temperature and then incubated with an anti-BrdU antibody (Abcam) diluted in 3% normal goat serum and 0.4% Triton on a shaker overnight at 4°C. Secondary staining and mounting were performed as described above.

Histology slides were imaged on an LSM 880 confocal microscope with AiryScan (Zeiss) on Superresolution mode using a 63x objective for high resolution imaging and an LSM 700 confocal microscope (Zeiss) using 20x and 63x objectives for all other imaging experiments.

Fluorescent In Situ Hybridization (FISH): FISH experiments were performed using the RNAscope Multiplex Fluorescent Reagent Kit v2 assay (ACD Bio) as described by the manufacturer for fixed-frozen tissue, except tissue was not baked for 30 minutes at 60°C prior to tissue dehydration. Brains were embedded in OCT following 30% sucrose treatment and frozen at -80°C for a minimum of 1 day and then sliced in 15 um thick

coronal sections on a CryoStar NX70 Cryostat (Thermo Fisher) before being mounted on coverslips for downstream RNAscope processing. Mouse *Il1rl1* RNAscope Probe (ACD Bio, 440661) and TSA Plus Cyanine 3 reagent (Perkin Elmer) were used to detect *Il1rl1* transcript. For immunohistochemical labeling with antibodies following the RNAscope assay, tissues were incubated with blocking and antibody solutions as described above immediately after developing the HRP-TSA Plus signal and carefully washing four times.

Flow cytometry: For all flow cytometry experiments, animals were perfused transcardially with ice-cold 1X PBS and hippocampi were isolated under a dissecting microscope where meninges and excess myelin were removed. Antibodies are outlined in the Key Resource Table. Gating was based on fluorescence minus one (FMO) negative staining controls. All data analysis was performed using FlowJo^{TM} software.

For sorting neuronal nuclei, cells were isolated using a protocol modified from Jaegar et al., 2018. Hippocampi were isolated under a dissecting microscope and mechanically dissociated using a 2 mL glass tissue homogenizer (Kontes Glassware) on ice using five strokes of the loose pestle and ten strokes of the tight pestle in nuclei isolation media (250 mM sucrose, 25 mM KCl, 5 mM $MgCl_2$, 10 mM Tris pH 8.0, and nuclease free H_2O). Dissociated nuclei were pelleted in an eppendorf tube at 1000 g for 5 minutes at 4°C and then resuspended in nuclei storage buffer (166.5 mM sucrose, 5 mM $MgCl_2$, 10 mM Tris pH 8.0, and nuclease free H_2O) using a P1000 tip. Nuclei were again pelleted at 1000 g for 5 minutes at 4°C and resuspended in blocking buffer consisting of 1% (weight/volume) RNase-free BSA and 1X PBS. Cells were sorted on a BD Facs Aria III and gated on forward/side scatter, nuclei by Hoechst, NeuN (Millipore)

to identify neuronal nuclei, and Prox1 (BioLegend) and Ctip2 (BioLegend) to identify nuclei from dentate granule cells and CA1 pyramidal neurons. For select experiments, cFos (Santa Cruz Biotech) was used to identify activated neurons. For experiments with downstream qPCR and single-nuclei RNA sequencing, all reagents were treated with 0.2 U/uL of SUPERasein RNAse inhibitor (Thermo Fisher) and instruments and working surfaces treated with RNase Away surface decontaminant (Thermo Fisher). For experiments stratifying neuronal nuclei by Il33-mCherry expression, the mCherry positive population was gated using an mCherry negative control and then divided into 3 equal populations such that each gate comprised of 33.3% of the mCherry positive population.

For sorting microglia for downstream RNA-sequencing, cells were isolated as described (Galatro et al., 2017). Briefly, hippocampi were mechanically dissociated using a glass tissue homogenizer in isolation medium (HBSS, 15 mM HEPES, 0.6% glucose, 1 mM EDTA pH 8.0). Cells were filtered and then pelleted at 300 g for 5 minutes at 4°C before being resuspended in 22% Percoll (GE Healthcare) and centrifuged at 900 g for 20 minutes with acceleration set to 4 and deceleration set to 1 in order to remove cellular debris. Pelleted microglia were then washed with isolation medium and incubated in block solution consisting of anti-mouse CD16/32 antibody (Biolegend). Cells were sorted on a BD FACS Aria III and gated on forward/side scatter, live cells by Hoechst, CD11b-PE (eBioscience), and CD45-FITC (BioLegend) to isolate microglia.

For sorting multiple CNS cell-types in parallel for comparative qPCR, cells were isolated and fixed as described by Srinivasan et al., 2016. Hippocampi were roughly minced with a sterile razor blade, incubated in 1X Accutase (Millipore) at 4°C for 1 hour, pelleted at 2000 g for 1 minute, and resuspended in Hibernate A Low Fluorescence

medium (BrainBits). Cells were then lightly pelleted using a benchtop microcentrifuge and supernatant filtered through a 70 µm cell strainer into a FACS tube. 1 mL of Hibernate A media was then added to the cell pellet and slowly triturated with a P1000 tip. Cells were again lightly pelleted and supernatant was filtered into FACS tubes. This process was repeated 2 additional times. To remove excess myelin, cells were then resuspended in 22% Percoll diluted with Hibernate A and centrifuged at 900 g for 20 minutes with acceleration set to 4 and deceleration set to 1. To fix and permeabilize cells, cell pellets were resuspended in 500 uL of Hibernate A and 500 uL of ice cold 100% ethanol was slowly added. Cells were incubated on ice for 15 minutes, washed twice with Hibernate A, and then incubated in block solution consisting of anti-mouse CD16/32 antibody (Biolegend). Cells were sorted on a BD FACS Aria III and gated on forward/side scatter, intact cells by Hoechst, CD11b (eBioscience) to identify microglia, GFAP (Millipore) to identify astrocytes, Olig2 (Thermo Fisher) to identify oligolineage cells, and NeuN (Millipore) to isolate neurons.

Single nuclei RNA-sequencing: Neuronal nuclei were isolated from hippocampus, stained with Alexa Fluor 488 mouse anti-NeuN 1:1500 (Millipore), and sorted on an Aria III (BD) flow cytometer. To account for "dropouts", we also isolated NeuN+ neuronal nuclei from *Il33^{mCherry/+}* mice and sorted the top 30% of mCherry+ neurons by intensity and sequenced them as metadata. FACS purified neuronal nuclei were sequenced using the Chromium single cell gene expression platform (10x Genomics, version 2). Approximately 15,000 nuclei from each sample were loaded into each well of Chromium Chip A according to the manufacturer instructions and combined into droplets with barcoded

beads using the Chromium controller. Libraries were prepared by the Gladstone Institutes Genomics Core following the instructions in the Chromium Single Cell 3' Reagent Kits version 2 user guide. The samples were sequenced to an average depth of 40,000-60,000 reads on an Illumina HiSeq 4000 sequencer.

Single nuclei data analysis: Sequenced samples were processed using the Cell Ranger 2.1 pipeline and aligned to the GRCm38 (mm10) mouse reference genome. In order to count the numerous intronic reads aligned from our nuclear dataset, a custom pre-mRNA GTF file was made using cellranger by converting the "transcript" annotation in the reference genome to "exon", enabling CellRanger to count pre-mRNAs. Clustering and differential expression analysis were conducted using Seurat version 2.3.4. Cells with fewer than 500 detected genes/cell or over 3000 genes/cell, comprising the lower and upper 5% of cells respectively, or more than 1% mitochondrial DNA were excluded during quality control steps before identification of variable genes in the dataset, cell centering, and scaling. Additionally, 3000 genes were eliminated that were expressed by fewer than 5 cells in the dataset.

After log normalization and scaling the data with a scale factor of 10,000, approximately 1500 of the most variable genes were identified and used for calculating nearest neighbors, PCA, and t-SNE plots. The most variable genes were identified using a LogVMR function from the Seurat package with parameters of expression mean between 0.125 and 5, and dispersion > 0.5. 40 PCs were calculated using these genes and the first 15 principle components were used for subsequent calculations. Clustering and t-SNE plots were computed using Seurat (Butler et al., 2018; Satija et al., 2015). A

resolution of 0.5 was used to generate clusters, and the clusters were named based on expression of canonical marker genes for each region of the hippocampus. For differential expression analysis of the dentate gyrus, cells from the two clusters identified in the dentate gyrus (0, 2) were extracted from the dataset, re-normalized, and scaled. The top 3000 most variable genes were calculated using the LogVMR method in Seurat; only genes with mean expression between 0.1 and 5 and dispersion over 0.1 were included in subsequent calculations. The cells were then clustered as described for the full dataset. Cells were identified as "female" or "male" based on their expression of the gene *Xist*; any cells expressing one or more counts of *Xist* were labelled female, while all others were labelled male. Female cells from sample 3 were known to express IL-33 based on IL-33mCherry fluorescence during sorting prior to sequencing. Differentially expressed genes were identified using the "FindMarkers" function in Seurat, comparing the cluster enriched in sorted IL-33 expressing cells with the other dentate gyrus cell cluster. Only genes expressed in 25% of the cells in a given cluster that pasted a log fold change threshold of 0.25 were included in the differentially expressed gene list. GO analysis was conducted using the Metascape webpage (www.metascape.org).

Bulk RNA sequencing: Microglia were isolated from hippocampus, stained with CD45-FITC 1:100 (BioLegend) and CD11b-APC 1:100 (BioLegend), and sorted on an Aria III (BD) flow cytometer into RLT plus buffer (Qiagen). RNA was extracted and purified using an RNeasy Mini Kit (Qiagen). RNA quality was measured using the Agilent RNA 6000 Pico kit on an Agilent Bioanalyzer. All samples had RNA Integrity Number (RIN) >7. For each sample, 10 ng of RNA was used as input for cDNA amplification and library

construction using the QuantSeq 3' mRNA-Seq Library Prep Kit FWD for Illumina (Lexogen) following manufacturer's instructions. Library quality and quantity was assessed using the Agilent High Sensitivity DNA kit on an Agilent Bioanalyzer and Quant-iT™ dsDNA Assay Kit on a Qubit Fluorometer (Thermo Fisher Scientific). Single-end (65-bp reads) sequencing was performed using an Illumina HiSeq 4000 yielding 30–45 million reads per sample.

Bulk RNA sequencing analysis: Quality of reads was evaluated using FastQC (http://www.bioinformatics.babraham.ac.uk/projects/fastqc), all samples passed quality control, and reads were aligned to mm10 (GRCm38; retrieved from Ensembl, version November 2019) using STAR (version 2.5.4b) (Dobin et al., 2013) with '--outFilterMultimapNmax 1' to only keep reads that map one time to the reference genome. Mapped reads were counted using HTSeq (version 0.9.0)(Anders et al., 2015) and DESeq2 package (version 1.24.0) (Love et al., 2014) was used to normalize the raw counts and perform differential gene expression analysis (using the apeglm method (Zhu et al., 2019) for effect size shrinkage). Volcano plot was made using genes from the comparison IL-33 vs PBS with adjusted p-value < 0.01 with the EnhancedVolcano package (version 1.2.0).

Behavioral Assays: Conditioned fear was elicited by administering three mild footshocks (0.75 mA) following a five-minute exposure to an array of contextual cues (conditioning chamber, chamber lights, white noise, scent of anise extract). Retrieval of the fear memory was assessed by a three-minute re-exposure of the animal to the conditioning

context in the absence of shock and freezing (the cessation of all movement outside of respiration) was interpreted as expression of fear memory. Video recordings were acquired and scored automatically in FreezeFrame (Actimetrics). Mice were habituated to transport and holding in a separate room for at least one hour prior to all conditioning or retrieval sessions and subjected to three days of handling prior to all behavioral tests. For assessment of fear discrimination, freezing was measured in a context similar to the conditioning context two hours later, but with the following variations: the chamber fan was turned off, the scent of anise extract was swapped for lemon extract, and a plastic divider was inserted to make the chamber walls circular and opaque. Freezing in the similar context was tested two hours following retrieval testing in the original conditioning context, and animals were rested in a holding room between sessions.

Anxiety-like behaviors were assessed via ten-minute exposures to the open field test (OFT) and five minute exposures to the elevated plus maze (EPM). Video recordings were acquired in Ethovision (Noldus) and time spent in the periphery of the OFT and in the closed arms of the EPM were scored through automated object detection and interpreted as anxiety-like behavior. Freezing and anxiety-like behaviors were both scored via an automated, unbiased process and all behavioral testing and analysis was performed blinded to genotype.

Slice Preparation and Patch-Clamp Electrophysiology: After euthanizing mice with 4% isoflurane and removing brains, 300 mm-thick transverse slices were prepared in ice-cold sucrose cutting solution (234 mM sucrose, 2.5 mM KCl, 1.25 mM NaH2PO4, 10 mM MgSO4, 0.5 mM CaCl2, 26 mM NaHCO3, and 10 mM glucose, equilibrated with 95% O2

and 5% CO2, pH 7.4) using a Leica VT1200 microtome (Leica Microsystems). Hippocampal sections were incubated for an hour at 32-34°C and then at room temperate in artificial cerebrospinal fluid (aCSF; 126 mM NaCl, 2.5 mM KCl, 1.25 mM NaH2PO4, 1 mM MgCl2, 2 mM CaCl2, 26 mM NaHCO3, and 10 mM glucose, equilibrated with 95% O2 and 5% CO2, pH 7.4).

Recording electrodes were made from borosilicate glass with a resistance 4–5.5 MΩ when filled with intracellular solution (115 mM potassium gluconate, 11 mM KCl, 1 mM MgCl2, 1 mM CaCl2,10 mM HEPES, 11 mM EGTA, and 2 mM K$_2$ATP, pH adjusted to 7.35 with KOH; 286 mOsm). Series resistance was monitored in all recordings, and the recordings were excluded from analysis if the series resistance was > 33 MΩ or varied by more than 10%. Recordings were obtained using a MultiClamp 700B microelectrode amplifier (Molecular Devices, Sunnyvale, CA), digitized using Digidata 1550B (Molecular Devices), and acquired at 20 kHz using pClamp 10 software (Molecular Devices). Recordings were performed in voltage-clamp mode at a holding potential of -70 mV and obtained from visually identified mature granule cell neurons in the mid and outer granule cell layer of the dentate gyrus, which were confirmed by morphology and intrinsic membrane properties. In the presence of aCSF supplemented with 0.5 µm tetrodotoxin (TTX) and 50 µm picrotoxin, miniature excitatory post-synaptic currents (mEPSCs) were isolated and recorded for 5 minutes. mESPCs were analyzed using ClampFit (Molecular Devices) and MiniAnalysis (Synaptosoft) software. Experimenter was blinded to genotype.

qPCR: To extract RNA from cells isolated by FACS, freshly sorted cells were pelleted at 500 g for 10 minutes at 4° and then resuspended in RLT Plus buffer (Qiagen). Cells were vortexed and frozen for at least one day at -80° before being thawed on ice and processed for RNA using an RNeasy Mini Kit (Qiagen). Purified mRNA was converted to cDNA with the High Capacity cDNA Reverse Transcription kit (Life Technologies) and amplified using either the Fast SYBR Green Master Mix (Thermo Fisher) or TaqMan Gene Expression Master Mix (Thermo Fisher) and a 7900HT Fast Real-Time PCR System (Applied Biosystems).

Western blotting: Hippocampi were dissected from freshly perfused mouse brains and excess meninges and myelin removed under a dissecting microscope. Tissues were then flash frozen on dry ice and sonicated for 20 seconds in lysis buffer (50 mM tris-HCl, 1 mM EDTA, 150 mM NaCl, 1% NP-40, 0.5% sodium deoxycholate and 0.1% SDS). The sample was centrifuged for 10 minutes at 15,000 rpm at 4°C and the pellet was discarded. Samples were run on a denaturing gel and transferred to PVDF membrane, blocked with 5% milk in TBST for 1 hour at room temperature, incubated with Brevican antibody (BioLegend, MMS-5127) at 1:200 overnight at 4°C and secondary at room temperature for one hour, and developed with ECL plus.

BrdU quantification: BrdU+ NeuN+ cells in the granule cell layer in the DG were counted in every sixth coronal hemibrain section and the total from six sections were multiplied by six to estimate the number of adultborn neurons.

Dendritic Spine and Spine Head Filopodia quantification: Images were acquired with an LSM 880 Confocal Microscope with AiryScan (Zeiss) on Superresolution mode using a 63x objective (NA 1.4) with 5x optical zoom (0.03 um pixel size). Z-stacks were acquired at a step-size set at half the optical section and laser power and gain were consistent across all experiments. AiryScan processing was performed in Zen software (Zeiss) at a setting of 6 ("optimal" setting). Images were taken in the molecular layer of the DG. Dendritic spine density was quantified using ImageJ by measuring a distance of at least 15 μm along a dendritic branch and then counting dendritic spines. The experimenter was blinded to genotype for all quantifications. For experiments comparing IL-33 cKO, IL1RL1 cKO, and IL1RL1 i-cKO mice to controls, AAV9-Syn1-GFP virus was injected into P2-3 pups intracerebroventricularly at a dilution of 1:250 in sterile saline and mice were analyzed at 2-4 months of age.

For experiments stratifying dendritic spines and spine head filopodia by Il33-mCherry expression, the soma of sparsely labeled granule cells were imaged using a 20x objective with 16-bit depth and the position of each neuron was recorded. Dendritic spines for each neuron were imaged at 63x as described above. Mean fluorescent intensity for mCherry was then quantified in the nucleus using ImageJ and mCherry negative neurons were identified manually. For mCherry+ neurons, Il33-mCherry low and high neurons were designated as the bottom and top half of neurons by mCherry intensity, respectively. For these experiments, AAV9-Syn1-GFP virus was injected into P2-3 pups intracerebroventricularly at a dilution of 1:750 in sterile saline and mice were analyzed at 2 months of age.

Scholl analysis: Z-stacks were acquired from 60 μm thick coronal sections containing hippocampus with an LSM 700 Confocal microscope (Zeiss) using a 20x objective. Sholl analysis was performed in ImageJ using the simple neurite tracer plugin (https://imagej.net/Simple_Neurite_Tracer).

Aggrecan and Homer1 puncta quantification: Images were acquired with an LSM 880 Confocal Microscope with AiryScan on Superresolution mode using the same specifications as described above for dendritic spines. Aggrecan puncta were quantified using the Puncta Analyzer plugin (Ippolito and Eroglu, 2010) in ImageJ and thresholding was consistent for every image. For colocalization of Aggrecan and Homer1 puncta, images were analyzed with the Puncta Analyzer plugin with a minimum pixel specification of 4. Three images in the molecular layer were averaged per mouse for analysis.

Aggrecan engulfment: Z-stacks encompassing entire microglia were collected on an LSM 880 Confocal Microscope with AiryScan (Zeiss) on Superresolution mode using a 63x objective (NA 1.4) with 5x optical zoom (0.03 um pixel size); laser power and gain were consistent across all experiments. Images were analyzed using Imaris software (Bitplane) by creating a 3D surface rendering of individual microglia, which were thresholded to ensure microglia processes were accurately reconstructed and maintained consistent thereafter. The microglia rendering was used to mask the CD68 channel within that microglia, which was then 3D rendered, and the CD68 volume was subsequently used to mask the Aggrecan channel. Aggrecan engulfment per microglia was then calculated as the total volume of Aggrecan within the masked CD68 volume.

Microglia coverage: Images of Iba1 immunostaining were acquired on an LSM 700 Confocal microscope (Zeiss) using a 20x objective with 16-bit depth. Microglia coverage was quantified in ImageJ by first thresholding the Iba1 channel and then measuring the area of Iba1+ pixels and normalizing that value by the total area per field of view in the DG molecular layer. Thresholding was held consistent for each image.

QUANTIFICATION AND STATISTICAL ANALYSIS

Graphpad Prism 8.3.0 was used for most statistical analyses. Statistical tests are as described in text and figure legends. Violin plots were used for data with $n \geq 20$ to better visualize the distribution of individual data points. RNA-sequencing data was analyzed in R as described in the methods section above.

References

Adlaf, E.W., Vaden, R.J., Niver, A.J., Manuel, A.F., Onyilo, V.C., Araujo, M.T., Dieni, C. V, Vo, H.T., King, G.D., Wadiche, J.I., et al. (2017). Adult-born neurons modify excitatory synaptic transmission to existing neurons. Elife *6*.

Alvarez, D.D., Giacomini, D., Yang, S.M., Trinchero, M.F., Temprana, S.G., Büttner, K.A., Beltramone, N., and Schinder, A.F. (2016). A disynaptic feedback network activated by experience promotes the integration of new granule cells. Science (80-.). *354*, 459–465.

Attardo, A., Fitzgerald, J.E., and Schnitzer, M.J. (2015). Impermanence of dendritic spines in live adult CA1 hippocampus. Nature *523*, 592–596.

Barbolina, M. V., and Stack, M.S. (2008). Membrane type 1-matrix metalloproteinase: Substrate diversity in pericellular proteolysis. Semin. Cell Dev. Biol. *19*, 24–33.

Basu, R., Duan, X., Taylor, M.R., Martin, E.A., Muralidhar, S., Wang, Y., Gangi-Wellman, L., Das, S.C., Yamagata, M., West, P.J., et al. (2017). Heterophilic Type II Cadherins Are Required for High-Magnitude Synaptic Potentiation in the Hippocampus. Neuron *96*, 160-176.e8.

Bednarek, E., and Caroni, P. (2011). β-Adducin is required for stable assembly of new synapses and improved memory upon environmental enrichment. Neuron *69*, 1132–1146.

Bennett, F.C., and Molofsky, A. V. (2019). The immune system and psychiatric disease:

a basic science perspective. Clin. Exp. Immunol. cei.13334.

Bergami, M., Masserdotti, G., Temprana, S.G., Motori, E., Eriksson, T.M., Göbel, J., Yang, S.M., Conzelmann, K.-K., Schinder, A.F., Götz, M., et al. (2015). A critical period for experience-dependent remodeling of adult-born neuron connectivity. Neuron *85*, 710–717.

Bessa, J., Meyer, C.A., de Vera Mudry, M.C., Schlicht, S., Smith, S.H., Iglesias, A., and Cote-Sierra, J. (2015). Altered subcellular localization of IL-33 leads to non-resolving lethal inflammation. J. Autoimmun. *55*, 33–41.

Bolós, M., Perea, J.R., Terreros-Roncal, J., Pallas-Bazarra, N., Jurado-Arjona, J., Ávila, J., and Llorens-Martín, M. (2018). Absence of microglial CX3CR1 impairs the synaptic integration of adult-born hippocampal granule neurons. Brain. Behav. Immun. *68*, 76–89.

Bonnans, C., Chou, J., and Werb, Z. (2014). Remodelling the extracellular matrix in development and disease. Nat. Rev. Mol. Cell Biol. *15*, 786–801.

Breton-Provencher, V., Bakhshetyan, K., Hardy, D., Bammann, R.R., Cavarretta, F., Snapyan, M., Côté, D., Migliore, M., and Saghatelyan, A. (2016). Principal cell activity induces spine relocation of adult-born interneurons in the olfactory bulb. Nat. Commun. *7*.

Cai, D.J., Aharoni, D., Shuman, T., Shobe, J., Biane, J., Song, W., Wei, B., Veshkini, M., La-Vu, M., Lou, J., et al. (2016). A shared neural ensemble links distinct contextual memories encoded close in time. Nature *534*, 115–118.

Danielson, N.B., Kaifosh, P., Zaremba, J.D., Hen, R., Losonczy, A., and Correspondence, M.A.K. Distinct Contribution of Adult-Born Hippocampal Granule Cells to Context Encoding.

Denny, C.A., Kheirbek, M.A., Alba, E.L., Tanaka, K.F., Brachman, R.A., Laughman, K.B., Tomm, N.K., Turi, G.F., Losonczy, A., and Hen, R. (2014). Hippocampal memory traces are differentially modiulated by experience, time, and adult neurogenesis. Neuron *83*, 189–201.

Dranovsky, A., Picchini, A.M., Moadel, T., Sisti, A.C., Yamada, A., Kimura, S., Leonardo, E.D., and Hen, R. (2011). Experience Dictates Stem Cell Fate in the Adult Hippocampus. Neuron *70*, 908–923.

Duan, X., Krishnaswamy, A., Laboulaye, M.A., Liu, J., Peng, Y.R., Yamagata, M., Toma, K., and Sanes, J.R. (2018). Cadherin Combinations Recruit Dendrites of Distinct Retinal Neurons to a Shared Interneuronal Scaffold. Neuron *99*, 1145-1154.e6.

Eyo, U.B., Peng, J., Swiatkowski, P., Mukherjee, A., Bispo, A., and Wu, L.-J. (2014). Neuronal Hyperactivity Recruits Microglial Processes via Neuronal NMDA Receptors and Microglial P2Y12 Receptors after Status Epilepticus. J. Neurosci. *34*, 10528–10540.

Eyo, U.B., Gu, N., De, S., Dong, H., Richardson, J.R., and Wu, L.J. (2015). Modulation of microglial process convergence toward neuronal dendrites by extracellular calcium. J. Neurosci. *35*, 2417–2422.

Favuzzi, E., Marques-Smith, A., Deogracias, R., Winterflood, C.M., Sánchez-Aguilera, A., Mantoan, L., Maeso, P., Fernandes, C., Ewers, H., and Rico, B. (2017). Activity-

Dependent Gating of Parvalbumin Interneuron Function by the Perineuronal Net Protein Brevican. Neuron *95*, 639-655.e10.

Finak, G., McDavid, A., Yajima, M., Deng, J., Gersuk, V., Shalek, A.K., Slichter, C.K., Miller, H.W., McElrath, M.J., Prlic, M., et al. (2015). MAST: a flexible statistical framework for assessing transcriptional changes and characterizing heterogeneity in single-cell RNA sequencing data. Genome Biol. *16*, 278.

Frischknecht, R., Heine, M., Perrais, D., Seidenbecher, C.I., Choquet, D., and Gundelfinger, E.D. (2009). Brain extracellular matrix affects AMPA receptor lateral mobility and short-term synaptic plasticity. Nat. Neurosci. *12*, 897–904.

Fu, A.K.Y.Y., Hung, K.-W.W., Yuen, M.Y.F.F., Zhou, X., Mak, D.S.Y.Y., Chan, I.C.W.W., Cheung, T.H., Zhang, B., Fu, W.-Y.Y., Liew, F.Y., et al. (2016). IL-33 ameliorates Alzheimer's disease-like pathology and cognitive decline. Proc. Natl. Acad. Sci. U. S. A. *113*, E2705-13.

Guo, N., Soden, M.E., Herber, C., TaeWoo Kim, M., Besnard, A., Lin, P., Ma, X., Cepko, C.L., Zweifel, L.S., and Sahay, A. (2018). Dentate granule cell recruitment of feedforward inhibition governs engram maintenance and remote memory generalization.

Han, J.-H., Kushner, S.A., Yiu, A.P., Cole, C.J., Matynia, A., Brown, R.A., Neve, R.L., Guzowski, J.F., Silva, A.J., and Josselyn, S.A. (2007). Neuronal Competition and Selection During Memory Formation. Science (80-.). *316*, 457–460.

Hanawa-Suetsugu, K., Itoh, Y., Ab Fatah, M., Nishimura, T., Takemura, K., Takeshita,

K., Kubota, S., Miyazaki, N., Wan Mohamad Noor, W.N.I., Inaba, T., et al. (2019). Phagocytosis is mediated by two-dimensional assemblies of the F-BAR protein GAS7. Nat. Commun. *10*, 4763.

Ibi, D., Takuma, K., Koike, H., Mizoguchi, H., Tsuritani, K., Kuwahara, Y., Kamei, H., Nagai, T., Yoneda, Y., Nabeshima, T., et al. (2008). Social isolation rearing-induced impairment of the hippocampal neurogenesis is associated with deficits in spatial memory and emotion-related behaviors in juvenile mice. J. Neurochem. *105*, 921–932.

Jaeger, B.N., Linker, S.B., Parylak, S.L., Barron, J.J., Gallina, I.S., Saavedra, C.D., Fitzpatrick, C., Lim, C.K., Schafer, S.T., Lacar, B., et al. (2018). A novel environment-evoked transcriptional signature predicts reactivity in single dentate granule neurons. Nat. Commun. *9*, 3084.

Josselyn, S.A., and Tonegawa, S. (2020). Memory engrams: Recalling the past and imagining the future. Science (80-.). *367*.

Kaneko, M., Stellwagen, D., Malenka, R.C., and Stryker, M.P. (2008). Tumor Necrosis Factor-α Mediates One Component of Competitive, Experience-Dependent Plasticity in Developing Visual Cortex. Neuron *58*, 673–680.

Kelley, K.W., Nakao-Inoue, H., Molofsky, A. V, and Oldham, M.C. (2018). Variation among intact tissue samples reveals the core transcriptional features of human CNS cell classes. Nat. Neurosci. *21*, 1171–1184.

Kelwick, R., Desanlis, I., Wheeler, G.N., and Edwards, D.R. (2015). The ADAMTS (A Disintegrin and Metalloproteinase with Thrombospondin motifs) family. Genome Biol.

16, 113.

Kempermann, G., Kuhn, H.G., and Gage, F.H. (1997). More hippocampal neurons in adult mice living in an enriched environment. Nature *386*, 493–495.

Kheirbek, M.A., Tannenholz, L., and Hen, R. (2012). NR2B-Dependent Plasticity of Adult-Born Granule Cells is Necessary for Context Discrimination. J. Neurosci. *32*, 8696–8702.

Kitamura, T., Ogawa, S.K., Roy, D.S., Okuyama, T., Morrissey, M.D., Smith, L.M., Redondo, R.L., and Tonegawa, S. (2017). Engrams and circuits crucial for systems consolidation of a memory. Science (80-.). *356*, 73–78.

van der Laan, L.J., Döpp, E.A., Haworth, R., Pikkarainen, T., Kangas, M., Elomaa, O., Dijkstra, C.D., Gordon, S., Tryggvason, K., and Kraal, G. (1999). Regulation and functional involvement of macrophage scavenger receptor MARCO in clearance of bacteria in vivo. J. Immunol. *162*, 939–947.

Lacar, B., Linker, S.B., Jaeger, B.N., Krishnaswami, S., Barron, J., Kelder, M., Parylak, S., Paquola, A., Venepally, P., Novotny, M., et al. (2016). Nuclear RNA-seq of single neurons reveals molecular signatures of activation. Nat. Commun. *7*.

Lee, H., Brott, B.K., Kirkby, L.A., Adelson, J.D., Cheng, S., Feller, M.B., Datwani, A., and Shatz, C.J. (2014). Synapse elimination and learning rules co-regulated by MHC class i H2-Db. Nature *509*, 195–200.

Levy, A.D., Omar, M.H., and Koleske, A.J. (2014). Extracellular matrix control of

dendritic spine and synapse structure and plasticity in adulthood. Front. Neuroanat. *8*, 116.

Li, Y., Du, X.-F.F., Liu, C.-S.S., Wen, Z.-L.L., and Du, J.-L.L. (2012). Reciprocal regulation between resting microglial dynamics and neuronal activity in vivo. Dev. Cell *23*, 1189–1202.

Liu, X., Ramirez, S., Pang, P.T., Puryear, C.B., Govindarajan, A., Deisseroth, K., and Tonegawa, S. (2012). Optogenetic stimulation of a hippocampal engram activates fear memory recall. Nature *484*, 381.

Madry, C., Kyrargyri, V., Arancibia-Cárcamo, I.L., Jolivet, R., Kohsaka, S., Bryan, R.M., and Attwell, D. (2018). Microglial Ramification, Surveillance, and Interleukin-1β Release Are Regulated by the Two-Pore Domain K+ Channel THIK-1. Neuron *97*, 299-312.e6.

Mayer, J., Hamel, M.G., and Gottschall, P.E. (2005). Evidence for proteolytic cleavage of brevican by the ADAMTSs in the dentate gyrus after excitotoxic lesion of the mouse entorhinal cortex. BMC Neurosci. *6*, 52.

McAvoy, K.M., Scobie, K.N., Berger, S., Russo, C., Guo, N., Decharatanachart, P., Vega-Ramirez, H., Miake-Lye, S., Whalen, M., Nelson, M., et al. (2016). Modulating Neuronal Competition Dynamics in the Dentate Gyrus to Rejuvenate Aging Memory Circuits. Neuron *91*, 1356–1373.

McHugh, T.J., Jones, M.W., Quinn, J.J., Balthasar, N., Coppari, R., Elmquist, J.K., Lowell, B.B., Fanselow, M.S., Wilson, M.A., and Tonegawa, S. (2007). Dentate gyrus NMDA receptors mediate rapid pattern separation in the hippocampal network. Science

(80-.). *317*, 94–99.

Miller, S.M., and Sahay, A. (2019). Functions of adult-born neurons in hippocampal memory interference and indexing. Nat. Neurosci. *22*, 1565–1575.

Miyamoto, A., Wake, H., Ishikawa, A.W., Eto, K., Shibata, K., Murakoshi, H., Koizumi, S., Moorhouse, A.J., Yoshimura, Y., and Nabekura, J. (2016). Microglia contact induces synapse formation in developing somatosensory cortex. Nat. Commun. *7*, 1–12.

Molofsky, A.B., Savage, A.K., and Locksley, R.M. (2015). Interleukin-33 in Tissue Homeostasis, Injury, and Inflammation. Immunity *42*, 1005–1019.

Naba, A., Clauser, K.R., Ding, H., Whittaker, C.A., Carr, S.A., and Hynes, R.O. (2016). The extracellular matrix: Tools and insights for the "omics" era. Matrix Biol. *49*, 10–24.

Nakashiba, T., Cushman, J.D., Pelkey, K.A., Renaudineau, S., Buhl, D.L., McHugh, T.J., Barrera, V.R., Chittajallu, R., Iwamoto, K.S., McBain, C.J., et al. (2012). Young Dentate Granule Cells Mediate Pattern Separation, whereas Old Granule Cells Facilitate Pattern Completion. Cell *149*, 188–201.

Oh, M.M., Oliveira, F.A., and Disterhoft, J.F. (2010). Learning and aging related changes in intrinsic neuronal excitability. Front. Aging Neurosci. *2*.

Oray, S., Majewska, A., and Sur, M. (2004). Dendritic spine dynamics are regulated by monocular deprivation and extracellular matrix degradation. Neuron *44*, 1021–1030.

Orlando, C., Ster, J., Gerber, U., Fawcett, J.W., and Raineteau, O. (2012). Perisynaptic chondroitin sulfate proteoglycans restrict structural plasticity in an integrin-dependent

manner. J. Neurosci. *32*, 18009–18017.

Palmer, G., and Gabay, C. (2011). Interleukin-33 biology with potential insights into human diseases. Nat. Rev. Rheumatol. *7*, 321–329.

Pan, S., Mayoral, S.R., Choi, H.S., Chan, J.R., and Kheirbek, M.A. (2020). Preservation of a remote fear memory requires new myelin formation. Nat. Neurosci. *23*, 487–499.

Paolicelli, R.C., Bolasco, G., Pagani, F., Maggi, L., Scianni, M., Panzanelli, P., Giustetto, M., Ferreira, T.A., Guiducci, E., Dumas, L., et al. (2011). Synaptic pruning by microglia is necessary for normal brain development. Sci. (New York, NY) *333*, 1456–1458.

Park, S., Kramer, E.E., Mercaldo, V., Rashid, A.J., Insel, N., Frankland, P.W., and Josselyn, S.A. (2016). Neuronal Allocation to a Hippocampal Engram. Neuropsychopharmacology *41*, 2987–2993.

Parkhurst, C.N., Yang, G., Ninan, I., Savas, J.N., Yates, J.R., Lafaille, J.J., Hempstead, B.L., Littman, D.R., and Gan, W.-B. (2013). Microglia promote learning-dependent synapse formation through brain-derived neurotrophic factor. Cell *155*, 1596–1609.

Pfeiffer, T., Poll, S., Bancelin, S., Angibaud, J., Inavalli, V.V.G.K., Keppler, K., Mittag, M., Fuhrmann, M., and Nägerl, U.V. (2018). Chronic 2P-STED imaging reveals high turnover of dendritic spines in the hippocampus in vivo. Elife *7*.

Pignatelli, M., Ryan, T.J., Roy, D.S., Lovett, C., Smith, L.M., Muralidhar, S., and Tonegawa, S. (2019). Engram Cell Excitability State Determines the Efficacy of Memory

Retrieval. Neuron *101*, 274-284.e5.

Pikkarainen, T., Brännström, A., and Tryggvason, K. (1999). Expression of macrophage MARCO receptor induces formation of dendritic plasma membrane processes. J. Biol. Chem. *274*, 10975–10982.

Pizzorusso, T., Medini, P., Landi, S., Baldini, S., Berardi, N., and Maffei, L. (2006). Structural and functional recovery from early monocular deprivation in adult rats. Proc. Natl. Acad. Sci. U. S. A. *103*, 8517–8522.

Ramanathan, K.R., Ressler, R.L., Jin, J., and Maren, S. (2018). Nucleus reuniens is required for encoding and retrieving precise, hippocampal-dependent contextual fear memories in rats. J. Neurosci. *38*, 9925–9933.

Richards, D.A., Mateos, J.M., Hugel, S., De Paola, V., Caroni, P., Gähwiler, B.H., and McKinney, R.A. (2005). Glutamate induces the rapid formation of spine head protrusions in hippocampal slice cultures. Proc. Natl. Acad. Sci. U. S. A. *102*, 6166–6171.

Rowlands, D., Lensjø, K.K., Dinh, T., Yang, S., Andrews, M.R., Hafting, T., Fyhn, M., Fawcett, J.W., and Dick, G. (2018). Aggrecan directs extracellular matrix-mediated neuronal plasticity. J. Neurosci. *38*, 10102–10113.

Roy, D.S., Arons, A., Mitchell, T.I., Pignatelli, M., Ryan, T.J., and Tonegawa, S. (2016). Memory retrieval by activating engram cells in mouse models of early Alzheimer's disease. Nature *531*, 508–512.

Roy, D.S., Muralidhar, S., Smith, L.M., and Tonegawa, S. (2017). Silent memory engrams as the basis for retrograde amnesia. Proc. Natl. Acad. Sci. U. S. A. *114*, E9972–E9979.

Ryan, T.J., Roy, D.S., Pignatelli, M., Arons, A., and Tonegawa, S. (2015). Memory. Engram cells retain memory under retrograde amnesia. Science *348*, 1007–1013.

Sahay, A., Scobie, K.N., Hill, A.S., O'Carroll, C.M., Kheirbek, M.A., Burghardt, N.S., Fenton, A.A., Dranovsky, A., and Hen, R. (2011). Increasing adult hippocampal neurogenesis is sufficient to improve pattern separation. Nature *472*, 466–470.

Schafer, D.P., Lehrman, E.K., Kautzman, A.G., Koyama, R., Mardinly, A.R., Yamasaki, R., Ransohoff, R.M., Greenberg, M.E., Barres, B. a, and Stevens, B. (2012). Microglia sculpt postnatal neural circuits in an activity and complement-dependent manner. Neuron *74*, 691–705.

Segel, M., Neumann, B., Hill, M.F.E., Weber, I.P., Viscomi, C., Zhao, C., Young, A., Agley, C.C., Thompson, A.J., Gonzalez, G.A., et al. (2019). Niche stiffness underlies the ageing of central nervous system progenitor cells. Nature *573*, 130–134.

Sipe, G.O., Lowery, R.L., Tremblay, M.-&Egrave, Kelly, E.A., Lamantia, C.E., and Majewska, A.K. (2016). Microglial P2Y12 is necessary for synaptic plasticity in mouse visual cortex. Nat. Commun. *7*, 1–15.

Steadman, P.E., Xia, F., Ahmed, M., Mocle, A.J., Penning, A.R.A., Geraghty, A.C., Steenland, H.W., Monje, M., Josselyn, S.A., and Frankland, P.W. (2020). Disruption of Oligodendrogenesis Impairs Memory Consolidation in Adult Mice. Neuron *105*, 150-

164.e6.

Stevens, B., Allen, N.J., Vazquez, L.E., Howell, G.R., Christopherson, K.S., Nouri, N., Micheva, K.D., Mehalow, A.K., Huberman, A.D., Stafford, B., et al. (2007). The classical complement cascade mediates CNS synapse elimination. Cell *131*, 1164–1178.

Sun, X., Bernstein, M.J., Meng, M., Rao, S., Sørensen, A.T., Yao, L., Zhang, X., Anikeeva, P.O., and Lin, Y. (2020). Functionally Distinct Neuronal Ensembles within the Memory Engram. Cell.

Susuki, K., Chang, K.-J., Zollinger, D.R., Liu, Y., Ogawa, Y., Eshed-Eisenbach, Y., Dours-Zimmermann, M.T., Oses-Prieto, J.A., Burlingame, A.L., Seidenbecher, C.I., et al. (2013). Article Three Mechanisms Assemble Central Nervous System Nodes of Ranvier. Neuron *78*, 469–482.

Talabot-Ayer, D., Calo, N., Vigne, S., Lamacchia, C., Gabay, C., and Palmer, G. (2012). The mouse interleukin (II)33 gene is expressed in a cell type- and stimulus-dependent manner from two alternative promoters. J. Leukoc. Biol. *91*, 119–125.

Tashiro, A., Sandler, V.M., Toni, N., Zhao, C., and Gage, F.H. (2006). NMDA-receptor-mediated, cell-specific integration of new neurons in adult dentate gyrus. Nature *442*, 929–933.

Toni, N., Teng, E.M., Bushong, E.A., Aimone, J.B., Zhao, C., Consiglio, A., van Praag, H., Martone, M.E., Ellisman, M.H., and Gage, F.H. (2007). Synapse formation on neurons born in the adult hippocampus. Nat. Neurosci. *10*, 727–734.

Tønnesen, J., Inavalli, V.V.G.K., and Nägerl, U.V. (2018). Super-Resolution Imaging of the Extracellular Space in Living Brain Tissue. Cell *172*, 1108-1121.e15.

Tremblay, M.Ě., Lowery, R.L., and Majewska, A.K. (2010). Microglial interactions with synapses are modulated by visual experience. PLoS Biol. *8*.

Tsien, R.Y. (2013). Very long-term memories may be stored in the pattern of holes in the perineuronal net. Proc. Natl. Acad. Sci. U. S. A. *110*, 12456–12461.

Vainchtein, I.D., Chin, G., Cho, F.S., Kelley, K.W., Miller, J.G., Chien, E.C., Liddelow, S.A., Nguyen, P.T., Nakao-Inoue, H., Dorman, L.C., et al. (2018). Astrocyte-derived interleukin-33 promotes microglial synapse engulfment and neural circuit development. Sci. (New York, NY) *359*, 1269–1273.

Valenzuela, J.C., Heise, C., Franken, G., Singh, J., Schweitzer, B., Seidenbecher, C.I., and Frischknecht, R. (2014). Hyaluronan-based extracellular matrix under conditions of homeostatic plasticity. Philos. Trans. R. Soc. B Biol. Sci. *369*.

Végh, M.J., Rausell, A., Loos, M., Heldring, C.M., Jurkowski, W., van Nierop, P., Paliukhovich, I., Li, K.W., del Sol, A., Smit, A.B., et al. (2014a). Hippocampal extracellular matrix levels and stochasticity in synaptic protein expression increase with age and are associated with age-dependent cognitive decline. Mol. Cell. Proteomics *13*, 2975–2985.

Végh, M.J., Heldring, C.M., Kamphuis, W., Hijazi, S., Timmerman, A.J., Li, K.W., van Nierop, P., Mansvelder, H.D., Hol, E.M., Smit, A.B., et al. (2014b). Reducing hippocampal extracellular matrix reverses early memory deficits in a mouse model of

Alzheimer's disease. Acta Neuropathol. Commun. *2*, 76.

Villeda, S.A., Plambeck, K.E., Middeldorp, J., Castellano, J.M., Mosher, K.I., Luo, J., Smith, L.K., Bieri, G., Lin, K., Berdnik, D., et al. (2014). Young blood reverses age-related impairments in cognitive function and synaptic plasticity in mice. Nat. Med. *20*, 659–663.

de Vivo, L., Landi, S., Panniello, M., Baroncelli, L., Chierzi, S., Mariotti, L., Spolidoro, M., Pizzorusso, T., Maffei, L., and Ratto, G.M. (2013). Extracellular matrix inhibits structural and functional plasticity of dendritic spines in the adult visual cortex. Nat. Commun. *4*, 1484.

Wake, H., Moorhouse, A.J., Jinno, S., Kohsaka, S., and Nabekura, J. (2009). Resting microglia directly monitor the functional state of synapses in vivo and determine the fate of ischemic terminals. J. Neurosci. *29*, 3974–3980.

Wang, C., Yue, H., Hu, Z., Shen, Y., Ma, J., Li, J., Wang, X.D., Wang, L., Sun, B., Shi, P., et al. (2020). Microglia mediate forgetting via complement-dependent synaptic elimination. Science (80-.). *367*, 688–694.

Weinhard, L., di Bartolomei, G., Bolasco, G., Machado, P., Schieber, N.L., Neniskyte, U., Exiga, M., Vadisiute, A., Raggioli, A., Schertel, A., et al. (2018). Microglia remodel synapses by presynaptic trogocytosis and spine head filopodia induction. Nat. Commun. *9*, 1228.

Wyss-Coray, T. (2016). Ageing, neurodegeneration and brain rejuvenation. Nature *539*, 180–186.

Publishing Agreement

It is the policy of the University to encourage open access and broad distribution of all theses, dissertations, and manuscripts. The Graduate Division will facilitate the distribution of UCSF theses, dissertations, and manuscripts to the UCSF Library for open access and distribution. UCSF will make such theses, dissertations, and manuscripts accessible to the public and will take reasonable steps to preserve these works in perpetuity.

I hereby grant the non-exclusive, perpetual right to The Regents of the University of California to reproduce, publicly display, distribute, preserve, and publish copies of my thesis, dissertation, or manuscript in any form or media, now existing or later derived, including access online for teaching, research, and public service purposes.

DocuSigned by:

Phi Nguyen

A445786FC85544F...   Author Signature

5/7/2021

Date